WESTFÄLISCHE
WILHELMS-UNIVERSITÄT
MÜNSTER

INSTITUT FÜR KERNPHYSIK

Masterarbeit

Evaluation of the Isolation Criteria in pp Collisions at the LHC

Helena Horstmann

Erstgutachter: PD Dr. Christian Klein-Bösing
Zweitgutachter: Prof. Dr. Anton Andronic

— Januar 2019 —

Contents

Introduction

Research on the properties of the strong interaction has revealed the existence of the quark-gluon plasma (QGP), a state of matter at extremely high energy density, in which quarks and gluons are no longer confined to bound hadrons. According to phenomenological models, the energy densities in heavy-ion collisions are high enough to produce a QGP and, as such, provide an experimental environment for its study.

The only way to get information about the underlying processes in high energy collisions is to analyse the resulting particle yields measured by specialised detectors. Based on knowledge about particle production and decay mechanisms, the final state particles can be traced back and thus reveal information about the initial collision processes. The formation of a QGP is expected to clearly alter the final outcome of a collision, as it will affect quarks and gluons passing through. To measure the arising effects, it is desirable to find an observable that stays unchanged by the QGP production and therefore still contains information about the initial collision process. Such an observable would provide a reference for measuring final state effects of the QGP.

High energy (prompt) photons produced in the initial stages of the collision fulfil these criteria and are therefore subject to several studies. The problem with their measurement is the large background of photons that are produced in later stages of a collision, especially decay photons from neutral mesons. One method to extract prompt photons is the application of an isolation criterion, exploiting the fact that prompt photons are produced back-to-back with a parton jet and therefore no other high energy particles are expected in their vicinity.

The aim of this thesis is the application and evaluation of the different isolation criteria. Monte Carlo studies are performed in order to assess the criteria's efficiency and ability to reject decay photons. Furthermore, an invariant mass analysis is carried out in order to determine isolated decay photons from neutral mesons. Divided by the isolated cluster yield, such a measurement could be interpreted as a minimum contamination or purity estimation for the prompt photon yield.

Chapter 1 and 2 introduce the theory of the strong interaction, the quark-gluon plasma and experimental methods for its study. The experimental setup is described in chapter 3, followed by the presentation of the detailed analysis procedure in chapter 4. The final two chapters present the results; firstly from Monte Carlo productions (for validation), and secondly from real data.

1. Strong Interaction and a new State of Matter

Decades of research on the fundamental mechanisms and building blocks of nature has led to the idea of *elementary particles* constituting the observed material world[1]. These elementary particles can be divided into categories dependent on their internal properties. Hitherto, four different kinds of interaction have been observed between these particles. One is called the *strong force* and, after a brief introduction to the other forces and elementary particles, this chapter explores it in more detail.

1.1. Particles and their Interaction

The whole range of elementary particles can be seen in figure 1.1. A first distinction can be made between *fermions* and *bosons*, where these correspond to either half-integer or integer values (respectively) of a certain intrinsic property called *spin*. In principle, fermions can be thought of as the fundamental building blocks of

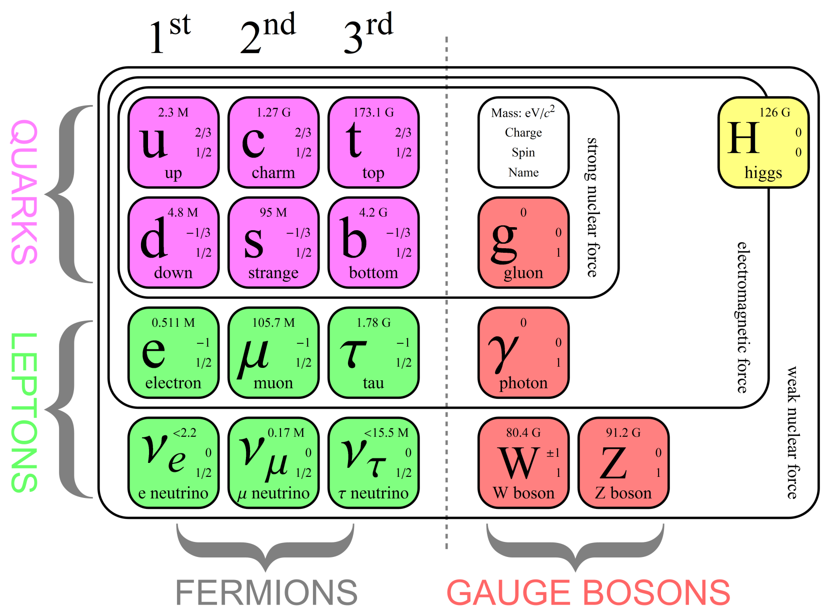

Figure 1.1.: Overview of the fundamental building blocks of matter in 2018. [Ser15]

[1] The term elementary simply refers to the fact that in case of a possible substructure, it has not been found so far.

matter, while gauge bosons work as mediators for the fermions[2]. There are three forces relevant on the scale of elementary particles: electromagnetism, the weak force and the aforementioned strong force. Each force couples to a certain kind of *physical charge* (for instance electric, weak or strong charge), which is an intrinsic particle property. A particle's ability to interact thus depends on how it is charged. Each force is thought to be mediated by the exchange of a corresponding *gauge boson*. Mathematically, such interactions can be described in terms of *quantum field theories*.

Fermions can be subdivided into *leptons* and *quarks*. Quarks, together with the gauge boson, the *gluon*, are participants of the strong interaction. The corresponding theory is called *quantum chromodynamics*.
The term lepton preceded the quark model and formerly referred to very light particles. Three leptons carry a negative charge (electron, muon, tau) and therefore, together with electrically charged quarks and the gauge boson, the photon, they are participants of electromagnetism.
Finally, the weak force acts on all fundamental particles, including the three types of neutrino, and is mediated by the W^+-, W^-- and Z-bosons. Electromagnetism and the weak interaction have been found to be two manifestations of the same force, which can be combined into the electroweak theory.

Quarks and leptons can be arranged into three generations. Each generation consists of particles with similar properties in terms of electric charge and spin; the masses of the particles, however, increase from one generation to the next. The number of elementary particles increases since corresponding to every particle in figure 1.1, there exists a particle with the same mass and spin but opposite physical charges (called its *anti-particle*)[3]. Outcomes of any interaction between two or more particles are restricted by conservation laws such as the conservation of energy, momentum or charge. [Gri10]

1.2. Quantum Chromodynamics

The theory of quantum chromodynamics (QCD) describes the interaction of quarks and gluons. The two lightest quarks are called the up- and down-quark and in different combinations they are found to constitute protons and neutrons. After having discovered the inner structure of nucleons, a third type of quark appeared rather unexpectedly and hence came to be known as the strange-quark. On top of this, three more types of quarks were discovered. The heavier the quark, the more energy necessary to produce and observe it.
A remarkable property of quarks is that they only seem to occur in bound states. *Baryons* consist of three quarks (qqq) or three anti-quarks ($\bar{q}\bar{q}\bar{q}$), whereas *mesons* are a combination of a quark and an anti-quark ($q\bar{q}$). Any compound particle state

[2] The Higgs Boson is an exception; it does not correspond to a force but, rather, to a scalar field, which is required to explain the mass of elementary particles.
[3] A particle can also be its own anti-particle, if the physical charges are zero.

consisting of quarks is categorised as a *hadron*.
Quantum chromodynamics offers an explanation for this particular behaviour by introducing the *colour charge*. The colour charge can be red, green or blue (along with their respective anti-colours respectively) and each quark carries one of these colours (while anti-quarks carry an anti-colour). The connection to colour theory can be made by assuming that all three colours combined result in a colourless 'white' state, which are the only observable in nature. Another way of forming a colourless state is to combine a colour with its anti-colour, which explains the existence of mesons. The fact that quarks (under normal conditions) only appear in compound hadron states is referred to as *colour confinement*.

Quantum chromodynamics has been formulated following the example of *quantum electrodynamics* (QED), which describes the coupling of photons to electrically charged particles. In QCD, electric charge is replaced by colour charge, which (due to its fundamentally different concept[4]) entails different properties for the corresponding gauge boson. The most striking consequence is the fact that the gauge boson in the strong interaction carries colour itself, thus allowing for eight different types of gluons, each carrying a combination of colour and anti-colour. This property enables the self-interaction of gluons, which is responsible for the very different behaviour of QCD in comparison to QED. Figure 1.2 demonstrates this difference by showing the elementary interaction vertices for both theories, where particles are represented by different types of lines. It can be seen that

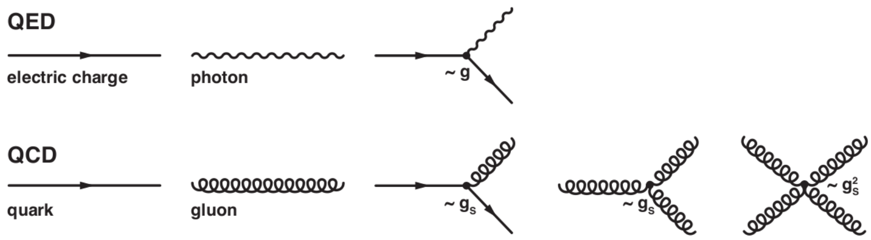

Figure 1.2.: Basic Feynman diagrams for QED and QCD. [KB13]

there is just one elementary type of interaction in QED that, dependent on the direction of time, can be interpreted as a charged particle emitting (or absorbing) a photon, or as a photon producing a particle anti-particle pair. More complicated processes in QED can be described by adding the same interaction vertex in various ways. Due to the self-interactions of gluons, QCD provides two additional elementary interaction vertices, making QCD more complex and giving rise to new effects. In principle, any process between particles can be imagined as arbitrarily more complex by including additional interaction vertices. An example of two Feynman diagrams describing the same process is given in figure 1.3. The probability of a process happening can be calculated by taking into account all possible Feynman diagrams describing that process, which is nearly impossible. However, the probability of an interaction is proportional to the *coupling constant* α of the corresponding force ($\alpha = \frac{g^2}{4\pi}$) and every vertex entails a factor of $\sqrt{\alpha}$.

[4]Electric charge is a scalar quantity and colour charge is described by quantum vectors

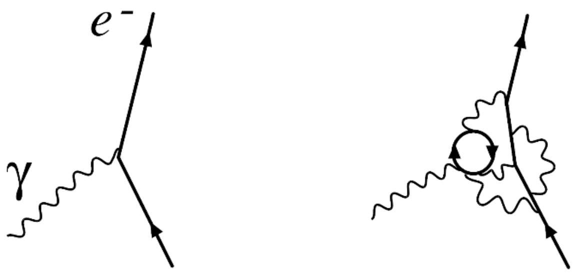

Figure 1.3.: Two Feynman diagrams depicting the same process in QED. [Ber06]

Where $\sqrt{\alpha} \ll 1$, processes with multiple interaction vertices are less likely to be realised. Consequently, the calculation of complicated diagrams with many interaction points only constitutes a negligibly small part of the actual result, and can thus be treated as higher order corrections to a process. This treatment is called *perturbation theory* and it can be applied in small couplings. The QED coupling constant at low energies is approximately $\frac{1}{137}$. Due to a decreasing screening effect by the polarised vacuum, the effective charge of a particle increases at shorter distances (higher energies), leading the coupling to slowly increase with energy. However, the effect is rather small and, at relevant scales, perturbation theory can be applied in QED. There is a similar screening effect in QCD, but the supplementary self-interaction of gluons leads to a further (and stronger) opposing reinforcement of the colour charge (anti-screening effect), causing the coupling to decrease with increasing energy (decreasing distances). [Ji]

Figure 1.4 demonstrates the general trend by evaluating various measurements at different collision energies (momentum transfers Q^2). It can be seen that,

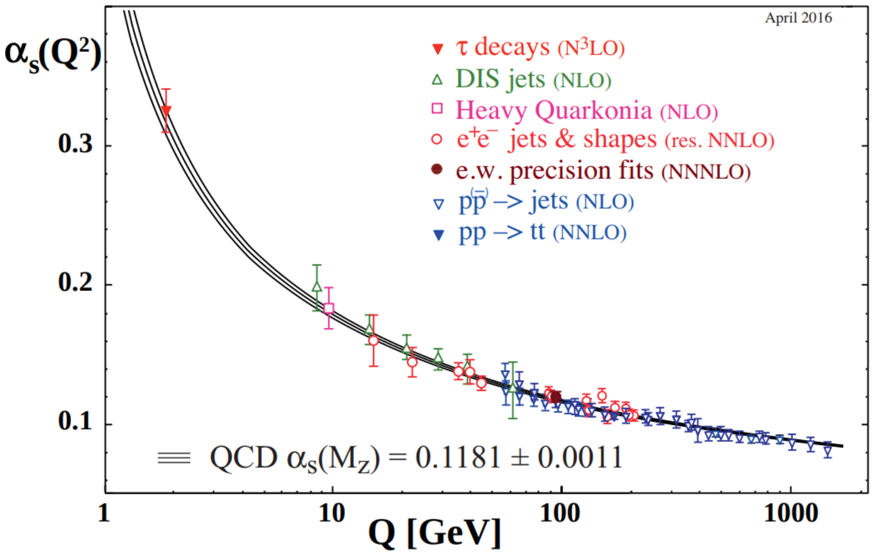

Figure 1.4.: Dependency of the running coupling constant α_s of the strong interaction on momentum transfer Q. [P⁺16]

in accordance with confinement, the coupling constant appears to diverge for large distances (small Q). The divergent trend of the coupling constant for low energies prohibits the application of perturbation theory in that regime and, as such, phenomenological and numerical approaches are used in order to predict the behaviour of low-energy QCD. One successful numerical approach simulates the theory on a discrete space-time lattice and is accordingly called *lattice* QCD.

At higher energies, the coupling constant decreases and eventually reaches a magnitude that allows for perturbative treatment (pQCD). The transition is marked by the strong scaling parameter Λ_{QCD}. The fact that the coupling constant of the strong interaction approaches zero at high energies has become known as *asymptotic freedom*, and implies that, during high energy transfers, quarks behave like free particles. [Gri10] [PRSZ06]

1.3. Phases of Hadronic Matter

Approaching baryonic matter thermodynamically, it is conceivable that, exceeding a certain energy density, the formation of hadrons might no longer exist. The investigation of a phase transition from confined hadronic matter to a *quark-gluon plasma* is subject to lattice QCD calculations. A schematic phase diagram of baryonic matter can be seen in figure 1.5. At small temperatures T and small

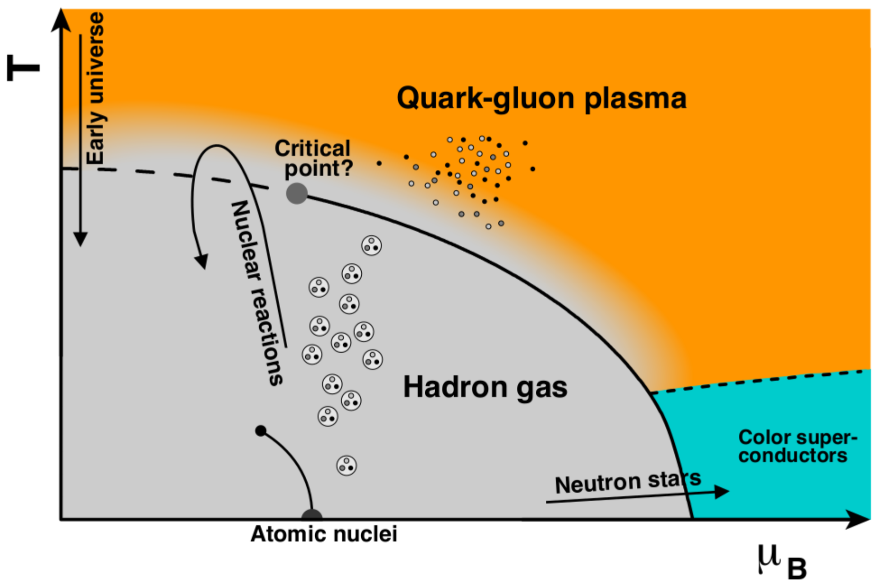

Figure 1.5.: Phase diagram of baryonic matter based on the prediction of different theoretical models. [KB13]

baryon densities μ_{b}, quarks and gluons exist as hadron gas. Starting with $\mu_{\mathrm{b}} = 0$ and increasing the temperature leads to a transition that inversely corresponds to the one our universe is thought to have gone through, a few microseconds after the big bang. As indicated in the diagram by the dashed line, the transition for low baryon densities is supposed to happen rather continuously. Lattice QCD calculations predict a transition temperature of $T_\mathrm{c} = (154 \pm 9)\,\mathrm{MeV}$ [B+12]. At around this temperature deconfinement starts; the coupling, however, is still too strong for perturbation theory to be applicable. An ideal QGP, allowing for perturbative treatment, is imaginable, but according to theoretical calculations not below $T \geq 5T_\mathrm{c}$ [Sat11]. Increasing the baryon density at small T first leads to a state that is thought to be existent inside neutron stars, until finally resulting in a colour super conducting phase and at high enough baryon densities perturbative treatment is again allowed [Hab18]. The transition in that regime is hard to access via established models and is therefore still subject to speculation. A possible well defined first order transition would require the existence of a critical point somewhere on the transition line. [KB13] [SS17]

2. Studying the Quark-Gluon Plasma via Prompt Photons

One opportunity to study the QGP, along with its transition at high temperatures and low baryon density, is provided by high energy heavy-ion collisions. However, the very short lifetime of $10^{-23}\,\mathrm{s}$ [Lod18] makes direct measurements of its properties impossible, and requires the precise evaluation of possible final state effects imprinted in the measurable particle production rate.

2.1. Heavy-Ion Collisions

In order to analyse the complex course of heavy-ion collisions, it is reasonable to take a look at the simpler proton-proton (pp) collisions first. In an imagined coordinate system, the colliding particles are thought to be moving along the z-axis. The interaction of two approaching protons can be categorized based on the occurring momentum transfer Q^2. At low Q^2 the protons are mainly expected to interact elastically, but as soon as $Q^2 \geq (2\,\mathrm{GeV/c})^2$ the energy is sufficient for the substructure to gain importance, and an inelastic interaction between nucleons can be traced back to an elastic scattering of its partons. Due to confinement, two back-to-back scattering partons will hadronise and form high energy particle *jets* that can be measured in corresponding detectors. Measured particles can be characterised by their mass and momentum. The momentum vector is conventionally split up into a transverse component, p_{T}, and a longitudinal one, p_{L}, in relation to the beam line (z-axis). p_{T} is invariant under Lorentz transformation along the z-direction and tightly bound to the momentum transfer of an interaction. Assuming all jet components could be measured and extracted from a given background, their total p_{T} would represent the transverse momentum of the original parton.

In principle, the collision of heavy nuclei is thought to behave similarly and is usually modeled as an incoherent superposition of nucleon-nucleon collisions. The particle production rate can then be estimated by the scaled results of pp collisions. The scaling factor corresponds to the number of binary inelastic nucleon-nucleon collisions within the heavy-ion collision, and therefore depends on the centrality of the collision. Based on that assumption, the difference in outcome compared to scaled pp collisions can be studied and interpreted as nuclear matter effects. Apart from the formation of the QGP itself, it is conceivable that *cold nuclear matter effects* occur due to the nucleon's position in a nucleus. Conclusions about the QGP based on final state effects in heavy-ion collisions can only be valid if the initial state effects are well understood. The cold nuclear matter effects are therefore studied in proton-lead collisions, in which the production of a QGP is not expected. Figure 2.1 shows the different collision systems and names the effects that they are supposed to study. An important observable to study nuclear matter

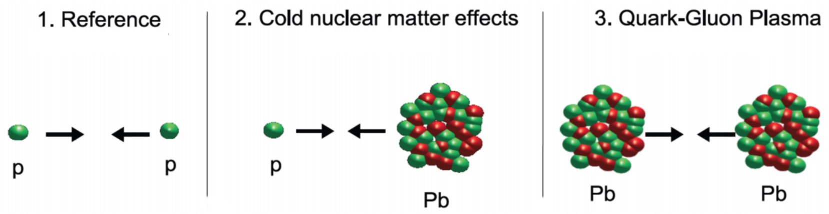

Figure 2.1.: Different collision systems for studying initial state effects in order to extract information about the QGP. [Zha16]

effects is the nuclear modification factor R_{AA} (R_{pA} for cold nuclear matter effects). It is defined as

$$R_{\mathrm{AA}} = \frac{\mathrm{d}^2 N_{\mathrm{AA}}/\mathrm{d}p_{\mathrm{T}}\mathrm{d}\eta}{\langle N_{\mathrm{coll}}\rangle \mathrm{d}N_{\mathrm{pp}}/\mathrm{d}p_{\mathrm{T}}\mathrm{d}\eta}, \tag{2.1}$$

where $d^2N_{\mathrm{AA}}/dp_{\mathrm{T}}d\eta$ and $d^2N_{\mathrm{pp}}/dp_{\mathrm{T}}d\eta$ represent the normalized particle yields and $\langle N_{\mathrm{coll}}\rangle$ the number of binary nucleon collisions per heavy-ion collision.

Before showing results for such a measurement, more theoretical aspects of the QGP formation should be discussed. The space-time evolution of a relativistic heavy-ion collision is depicted in figure 2.2. In the first stage of such a collision, hard scattering can occur and result in the production of parton jets. The dominant part of participating quarks and gluons heat up the region that is defined by the overlap of the two ions throughout the collision. This pre-equilibrium phase is thought to thermalise after the time τ_0, thus going over into the QGP state. A pressure gradient (due to the enormous temperatures) causes the medium to expand and cool down, so that after passing the critical temperature T_c the partons recombine and form a hadron gas. The hadron gas further expands until the *chemical freeze-out* at T_{ch} establishes the final hadron configurations that can be reconstructed with particle detector systems. The high energy parton jets, which were produced before the QGP state formed, will have to traverse the QGP and may lose energy due to interactions with it. This phenomenon has become known as *jet quenching*, and is regarded as a promising observable because a comparison to an unaffected jet spectrum could result in the determination of the particle's energy loss due to the QGP. The necessary comparative data could be taken from yield measurements in pp collisions, or obtained from perturbative QCD calculations of the initial hard scattering cross sections. Figure 2.3 demonstrates measurements of the nuclear modification factor in PbPb and pPb collisions for a range of particle types. It can be seen that hadrons are strongly suppressed in central PbPb collisions in comparison to the results of pp collisions, while there is no sign of clear suppression in pPb collisions. This indicates the interaction of partons with the QGP. The electromagnetic and weak gauge bosons do not

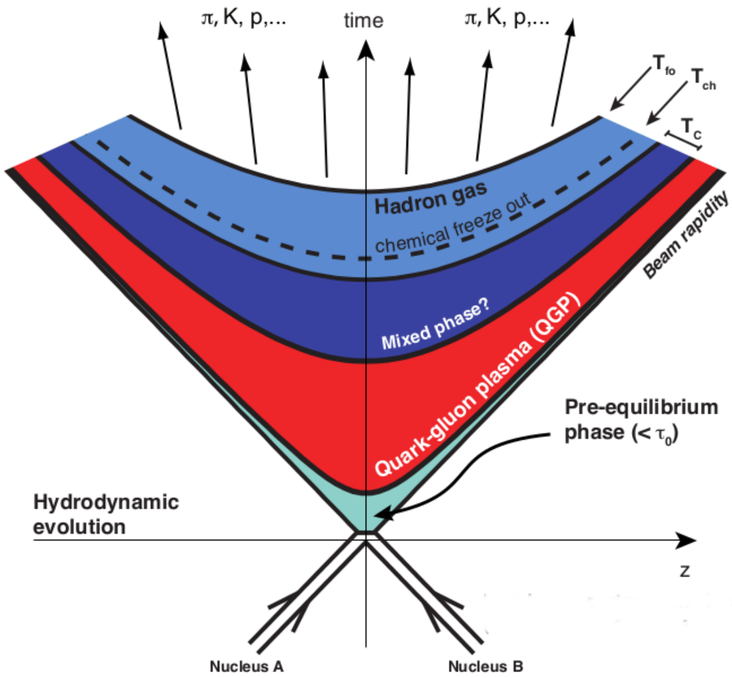

Figure 2.2.: Space-time evolution of a high energy heavy-ion collision, indicating the phase transitions the colliding quarks and gluons go through. [KB13]

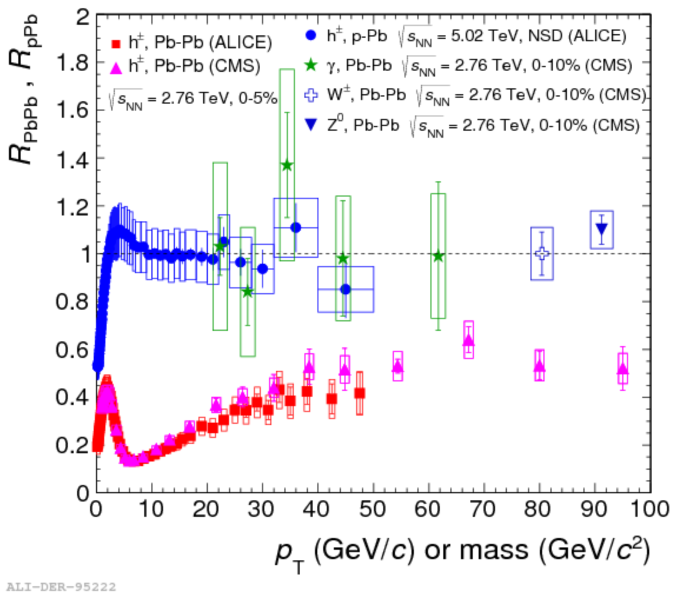

Figure 2.3.: Measurement of R_{PbPb} and R_{pPb} for hadrons and gauge bosons in pPb and central PbPb collisions. [Ben16]

show remarkable deviations from unity, meaning that their production in heavy-ion collisions behaves as expected by the nucleon scaling. Due to their lack of interaction with the QGP, a measurement of these observables can provide a validation of the superposition assumption in heavy-ion collisions. The infinite lifetime of photons in comparison to the massive weak gauge bosons, and the greater strength of the electromagnetic interaction, are the reasons why photons are generally easier to measure. The challenge in measuring photons, however, lies in their numerous production mechanisms. [KB13] [Lod18]

2.2. Photon Production Mechanisms

Photons are produced at all stages of a collision. Dependent on their production mechanism, they are divided into *direct* and *decay* photons. The term direct photons relates to a production time quite early in the collision; it covers *prompt* photons from initial hard scattering, *fragmentation* photons from jet fragmentation and *thermal* photons from QGP radiation.

Prompt photons are mostly produced back-to-back with a quark or gluon jet. The corresponding leading order Feynman diagrams of the main production processes are shown in figure 2.4. They depict quark gluon Compton scattering and quark

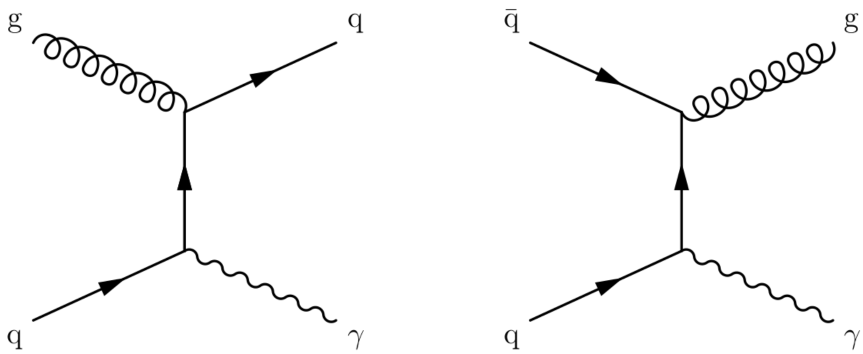

Figure 2.4.: The two leading order Feynman diagrams for prompt photon production. Left: quark gluon *Compton scattering*. Right: quark antiquark *annihilation*. [Lod18]

anti-quark annihilation. As prompt photons are produced in the very first stage of a collision before a QGP forms, they prove to be an ideal observable for probing the initial state effects of heavy-ion collisions in order to validate the $\langle N_{\text{coll}} \rangle$ scaling. Furthermore, so called γ-hadron correlation measurements employ the fact that prompt photons are produced back-to-back with a parton jet, in order to analyse the hadron's energy loss from traversing the QGP. But even independent of the QGP research, high energy prompt photon measurements provide a solid testing ground for pQCD calculations. Fragmentation photons arise during the jet fragmentation; figure 2.5 shows the production of a fragmentation photon next to the production of a prompt photon. Figure 2.6 shows the theoretical pQCD

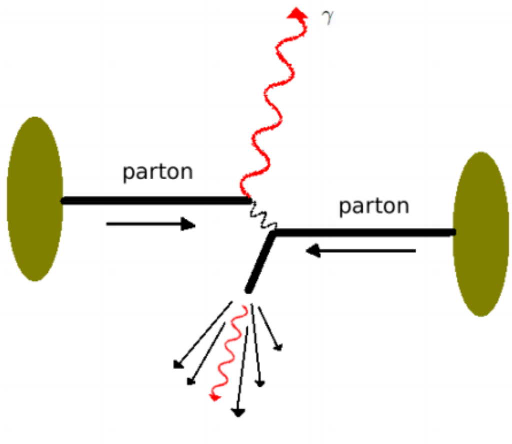

Figure 2.5.: Schematic view of fragmentation vs. prompt photon production. [Ron16]

predictions (including next-to-leading order [NLO] corrections) for the composition of the direct photon yield in pp collisions at $\sqrt{s} = 14\,\mathrm{TeV}$. It is noticeable that the

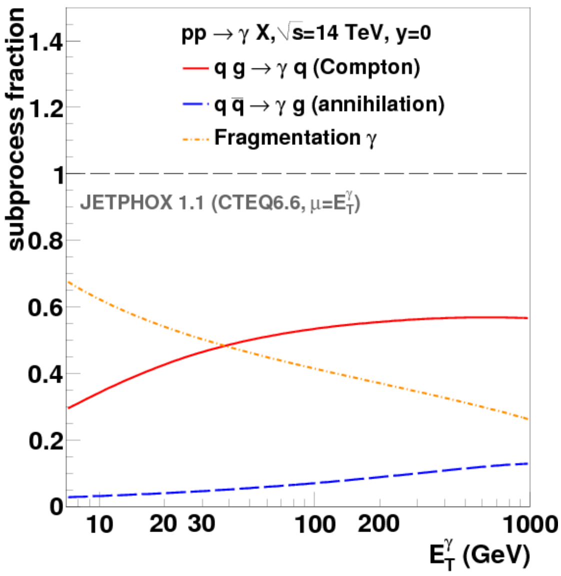

Figure 2.6.: Next-to-leading order pQCD calculations for the direct photon contributions in pp collisions at $\sqrt{s} = 14\,\mathrm{TeV}$. [Id10]

Compton scattering clearly dominates the annihilation process. Thermal photons are only produced in heavy-ion collisions as they are defined as radiation of the hot medium itself. They are expected to dominate the direct photon yields at low p_T ($p_T \lesssim 3\,\mathrm{GeV/c}$) and their study enables the determination of the temperature development of the QGP. The measurement of these photons provides a great opportunity to study established theories and QGP effects. The main problem with studying direct photons is the large background of decay photons caused by neutral meson decays. Neutral mesons are produced during the hadronisation processes of parton jets or in the case of a QGP with chemical freeze out. Most of the decay photons come from neutral pions (π^0) via their dominant two-photon decay channel. [A+18] [Lod18] [Id10] [B+14]

2.3. Isolation Criterion

An established method for extracting a prompt photon signal is to exploit the fact that prompt photons are produced back-to-back with a parton jet, and therefore no high p_T particles are expected in their vicinity. Decay or fragmentation photons, on the contrary, should primarily occur as part of hadron showers. The application of an *isolation cut* is therefore an established method to extract a prompt photon signal. A photon counts as isolated if, within a cone of radius R_iso around the photon, the hadronic activity does not exceed a threshold $p_\mathrm{T}^\mathrm{thresh}$. As such, an isolation criteria comprises two independent variables. The isolation radius is defined as

$$R_\mathrm{iso} = \sqrt{(\phi_\mathrm{i} - \phi_\gamma)^2 + (\eta_\mathrm{i} - \eta_\gamma)^2} \tag{2.2}$$

with ϕ_γ and η_γ representing the angles of the photon's (γ) detection in relation to the z-axis, and ϕ_i and η_i that of the i^th particle[5]. A schematic view of a possible isolation cone in relation to η and ϕ is portrayed in figure 2.7. The larger the

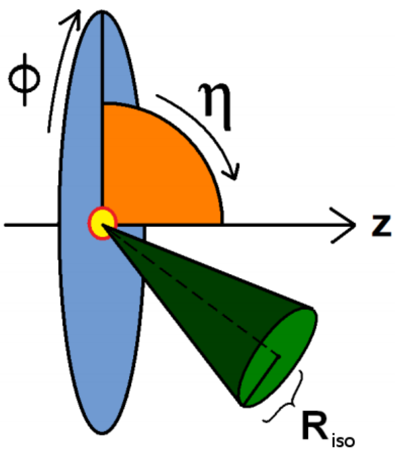

Figure 2.7.: Established coordinate system in high energy collisions. [Pop11]

value of R_iso chosen, the better the background rejection works. The size of the cone is constrained by the detector acceptance, however, since for every photon the cut is used on, the same conditions should apply. Therefore, the cone is not allowed to overlap the boundary of the used detectors. A typical value for the radius would be $R_\mathrm{iso} = 0.4$. The value for $p_\mathrm{T}^\mathrm{thresh}$ must be chosen low enough to ensure the rejection of high p_T decay photons, but high enough to allow for a small background from the underlying event. There are several approaches for the selection of an energy threshold; in this thesis, only the most common ones will

[5] η is actually called pseudorapidity and is solely dependent on the angle: $\eta = -\ln[\tan(\frac{\theta}{2})]$

be introduced. The hadronic activity in these criteria is represented by the sum of the p_{T} of the detected particles within the cone. The resulting measurable value will then be compared to $p_{\mathrm{T}}^{\mathrm{thresh}}$, which can either be fixed or dependent on the respective photon's p_{T}. Both criteria can be displayed as follows:

$$\sum^{cone} p_{\mathrm{T}} \leq p_{\mathrm{T}}^{\mathrm{thresh}} \tag{2.3}$$

and

$$\sum^{cone} p_{\mathrm{T}} \leq \epsilon p_{\mathrm{T}}^{\gamma}. \tag{2.4}$$

Typically, the value for a fixed threshold is chosen to be at least $p_{\mathrm{T}}^{thresh} < 2\,\mathrm{GeV/c}$ and the photon fraction as $\epsilon = 0.1$. [Lod18] [B+16a]

3. Experimental Setup

3.1. Large Hadron Collider (LHC)

In 1984, even before the actual large electron-positron collider (LEP) was ready to run, it was already thought that a new, more powerful collider could make use of the 27 km tunnel built for the LEP. The LEP started working in 1989 with an initial energy of 91 GeV, stopping in 2000 with an energy of 209 GeV to make way for the large hadron collider (LHC). [CER]
The LHC accelerates protons and heavy ions (lead and xenon nuclei). Protons are currently accelerated up to an energy of 6.5 TeV, resulting in a total collision energy of 13 TeV. For lead ions that would correspond to an energy of 5.02 TeV per nucleon pair. The acceleration path of a proton can be followed in figure 3.1. Ionized

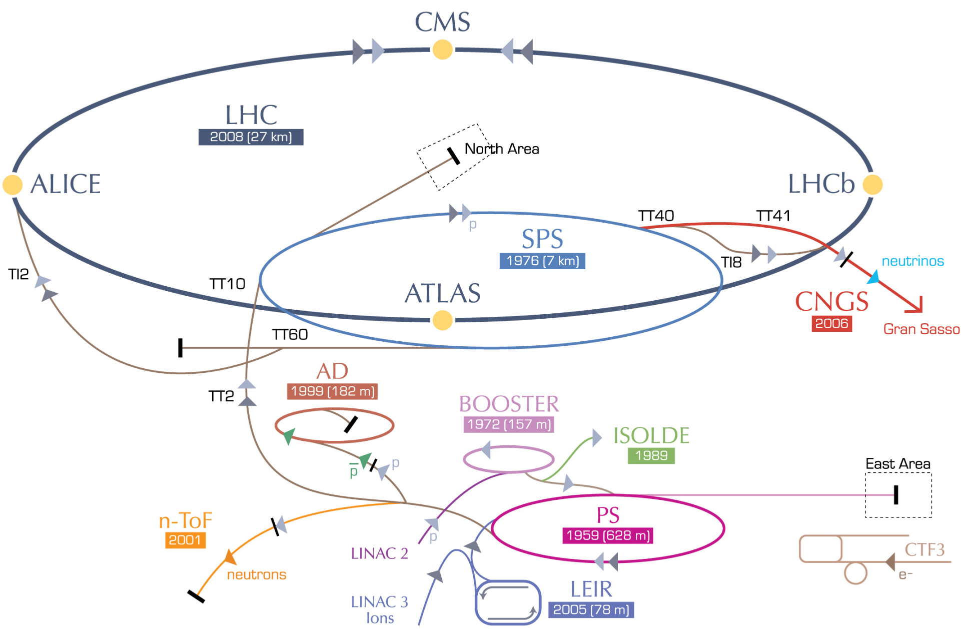

Figure 3.1.: Overview of the LHC, its pre-accelerator system and the four big experiments CMS, ALICE, ATLAS and LHCb. [CER06]

hydrogen serves as the proton source and the resulting protons are then accelerated by the linear accelerator Linac 2, providing an energy of 50 MeV. This proton beam is then transferred into the first synchrotron, called Booster, and leaves it with an energy of 1.4 GeV per proton. After passing two more accelerators, PS (Proton

Synchrotron) and SPS (Super Proton Synchrotron), the beam is injected into the LHC where it finally gains a total energy of 6.5 TeV per proton[6].

A strong magnetic field is necessary to keep the protons on their path around the accelerator. 1232 15 m long superconducting dipole electromagnets are used to drive the circular motion of the beam by generating magnetic fields of 8.3 T. Another set of 392 quadrupole magnets is used to focus the beam. The superconductivity requires the magnets to have a temperature of 1.85 K (even colder than the average temperature of the universe), which can be achieved by a cooling system of liquid helium. The LHC itself consists of two beam pipes so that proton beams can be injected in both directions. The beam is divided into so called *bunches* and collisions take place during bunch crossings at four different places around the accelerator, corresponding to the locations of the four big detectors built to process data produced by the collisions. [CER18]

The four experiments corresponding to the detectors (shown in figure 3.1 along the LHC circle) are CMS (Compact Muon Solenoid), ALICE (A Large Ion Collider Experiment), ATLAS (A Toroidal LHC ApparatuS) and LHCb (Large Hadron Collider beauty). CMS and ATLAS are two general-purpose detectors, constructed to explore new physics within the capacity the LHC provides. These collaborations study limits of the standard model such as the matter anti-matter imbalance, the search for dark matter candidates, and the relation between gravity and the other forces. As the two detectors use different technical setups to take in and process data, they can confirm each others discoveries. The discovery of the Higgs Boson in 2012 was a big success of these experiments and further recognition of the standard model. LHCb is a more specialised experiment, devoted to studying the difference between matter and anti-matter by focusing on the measurement of the beauty-quark. [Col18a] [Col18b] [CER13]
As this work is part of the ALICE experiment, it will be described in greater detail below.

3.2. A Large Ion Collider Experiment (ALICE)

The ALICE experiment is dedicated to the research of the QGP and its transition phase. PbPb collisions are analysed in comparison to pPb and pp collisions. In order to understand the processes of high energy collisions (especially heavy-ion collisions), it is necessary to collect as much information about the outcome as possible; this increases the chance of uncovering new insights into underlying physical processes. To achieve this, the ALICE detector consists of many subdetectors, each specialized to record certain particle properties. The whole detector system can be seen in figure 3.2. The individual subdetector systems (that are relevant for this thesis) and their functionalities will be described below.

[6]For heavy ions the process is slightly different in terms of energies and preaccelerators, but is the same in principle.

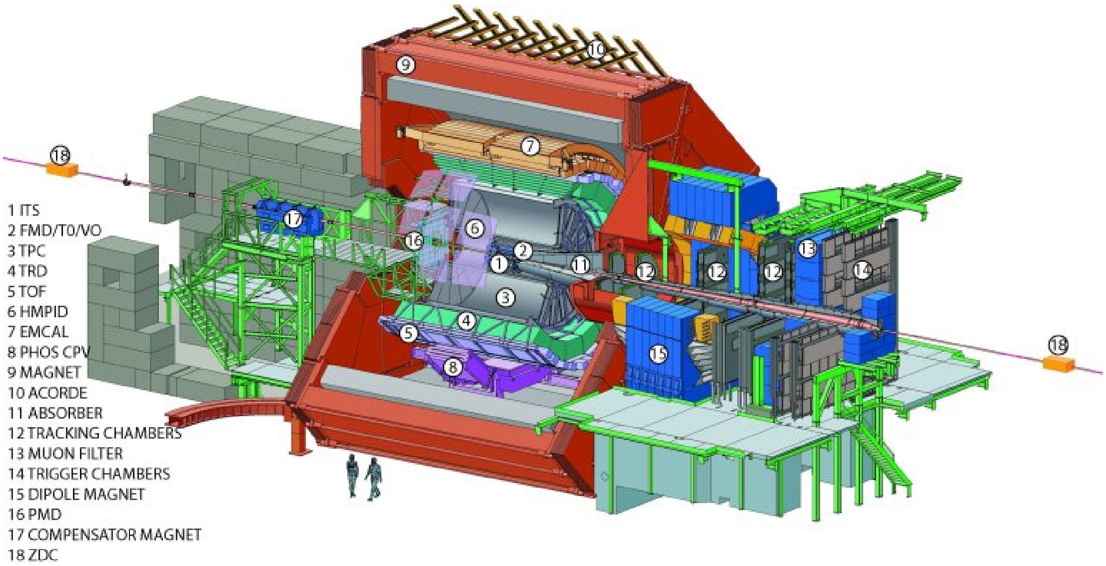

Figure 3.2.: Insight into the ALICE detector. [Col08]

3.2.1. Inner Tracking System (ITS) and V0 Detector

The ITS is a relatively small detector at the center of the detector complex, shown in figure 3.2 (no. 1). It is as close to the interaction point as technically possible and it consists of six layers of silicon detectors, placed coaxially around the beam line. The two inner layers are silicon pixel detectors (SPD) and they can be seen in yellow in figure 3.3, wrapped around the red beam pipe. The next two layers, shown in light blue, are silicon drift detectors (SDD), followed by two more layers of silicon strip detectors (SSD). The whole system covers a pseudorapidity range of $|\eta| \leq 0.9$ and its purposes include reconstructing primary and secondary vertices, keeping record of very short lived charged particles and improving the momentum and angle resolution of particles measured by the time projection chamber. [Man12]

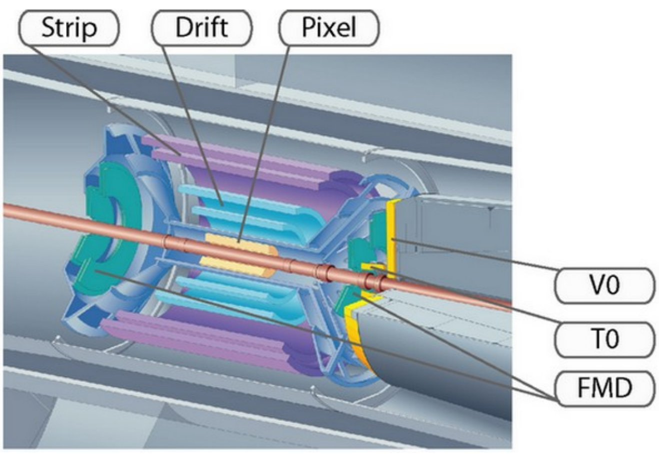

Figure 3.3.: Inner tracking system at the heart of the ALICE detector. [Man12]

Figure 3.3 also contains the three forward detectors called V0, T0 and FMD (Forward Multiplicity Detector). The T0 and V0 detectors are part of the ALICE trigger system, while the FMD can provide information about the charged particle multiplicities in forward direction. [C+04]
The V0 detector consists of two circular scintillating arrays surrounding the beamline; one covers a pseudorapidity range of $2.8 \leq \eta \leq 5.1$ (V0-A), the other $-3.7 \leq \eta \leq -1.7$ (V0-C). The detector is part of ALICE's *minimum bias* trigger (V0AND) system, which requires a coincidence of the bunch crossing signal and hits in both arrays. The task of the minimum bias trigger is to distinguish data arising from beam-beam interaction from possible data due to background noise, while keeping the readout of the collision as unbiased as possible. [A+13]

3.2.2. Time Projection Chamber (TPC)

The TPC is the main tracking device of the ALICE detector. The inner structure of the chamber can be seen in figure 3.4 and its relation to the whole detector system in figure 3.2 (no. 3). The chamber is filled with a gas mixture of

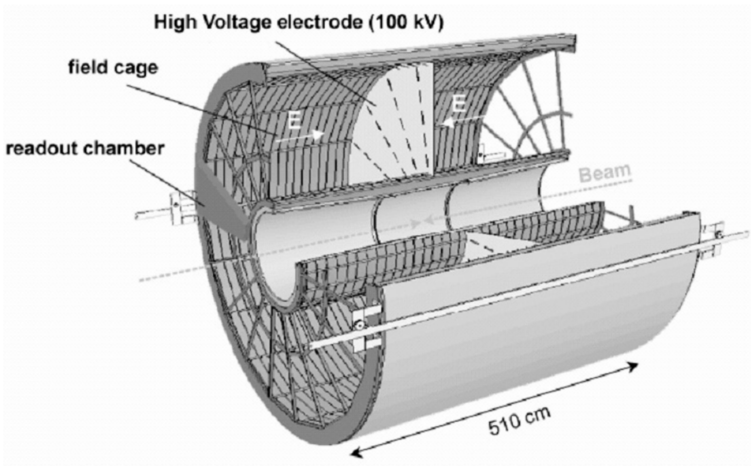

Figure 3.4.: Schematic view of the time projection chamber. [Rø09]

90% Ne and 10% CO_2 and divided into two parts, separated by a central electrode with high voltage. Charged particles going through the TPC will ionize the gas and the resulting free electrons move to the end plates of the TPC, where the corresponding energy loss can be measured by the readout chambers. A big solenoidal magnet surrounds the 'central barrel' detectors, creating a magnetic field of 0.5 T (figure 3.2, no. 9). The resulting curvature of a charged particle's trajectory in the magnetic field depends on the particle's momentum, while the energy loss contains information about the velocity; both together lead to the particle's mass, and therefore, ideally, to its identification. The TPC covers a pseudorapidity range of $|\eta| \leq 0.9$. [D+00]

3.3. Electromagnetic Calorimeter (EMCal)

As photons are electrically neutral, they cannot be detected by the two former mechanisms. The EMCal is based on a different detection method; it measures the energy of an incoming particle. The detector consists of many alternating layers of lead and scintillator material. If a high energy photon enters the detector, it can produce an electron-positron pair by interacting with the detector atoms. The likelihood of this process increases with the square of the atomic number of the material, so the lead layers ensure a high conversion probability. The produced electrons and positrons interact with the detector by emitting photons via bremsstrahlung, which can again convert into new electron-positron pairs. This process is called an *electromagnetic shower* and it continues until the energy of the produced particles is small enough to excite the scintillator layers, from where the signal will be led to avalanche photodiodes, converted into an electrical current, amplified, and read out.

The whole detector and its internal composition can be seen in figure 3.5, and its position in the detector in figure 3.2 (no. 7). The EMCal covers a pseudorapidity range of $|\eta| \leq 0.7$ and an azimuthal acceptance of $\Delta\phi = 107\,°$. It is placed 4.5 m from the beam line with a radial depth of 1.1 m. The inner structure of the

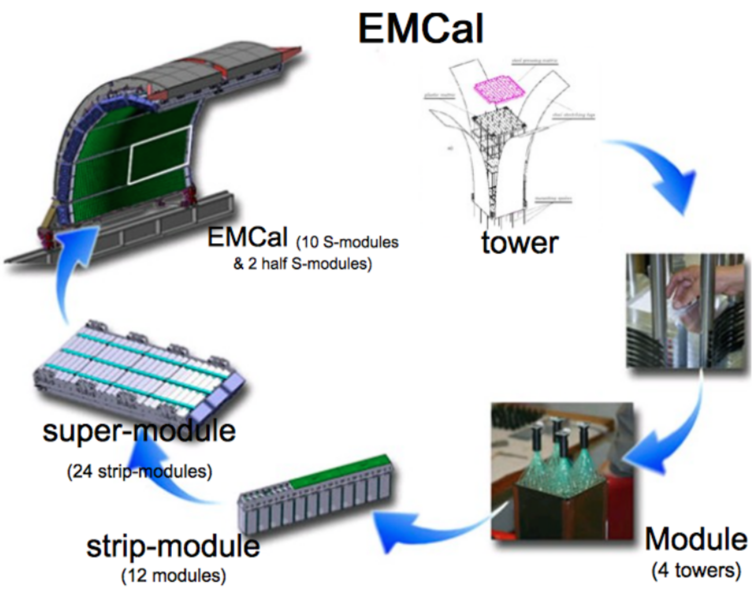

Figure 3.5.: Composition of the electromagnetic calorimeter. [Lod18]

EMCal is modular. One module contains 2×2 so called *towers*, each consisting of 76 alternating layers of 1.44 mm Pb and 77 layers of 1.76 mm scintillator. A row of 12 such modules constitutes a strip module, and 24 strip modules form a super module (12×24 modules). The EMCal comprises 10 such super modules and two smaller ones with a 4×24 module structure, so that in total the EMCal detector provides 12,288 towers (or cells). [C$^+$08] [A$^+$10]

Exploiting the ability to produce electromagnetic showers, the EMCal was mainly constructed to detect photons and electrons. However, long lived hadrons can deposit a part of their energy in the EMCal as well, contributing to the background of photon measurements.

3.3.1. EMCal Trigger System

Apart from detecting neutral particles, the EMCal also provides a trigger system that allows the identification and selection of rare events, such as the occurrence of high energy photons or jets. The EMCal trigger system has a hierarchical structure. There are two trigger levels (L0 and L1) for high energy deposits. The L0 trigger requires a positive signal from the minimum bias trigger, and the L1 trigger is based on a positive decision from the L0 trigger.

L0 Trigger

Each super module (SM) is divided into three trigger regions. In figure 3.6, the schematic view of an EMCal super module can be seen. Each region contains

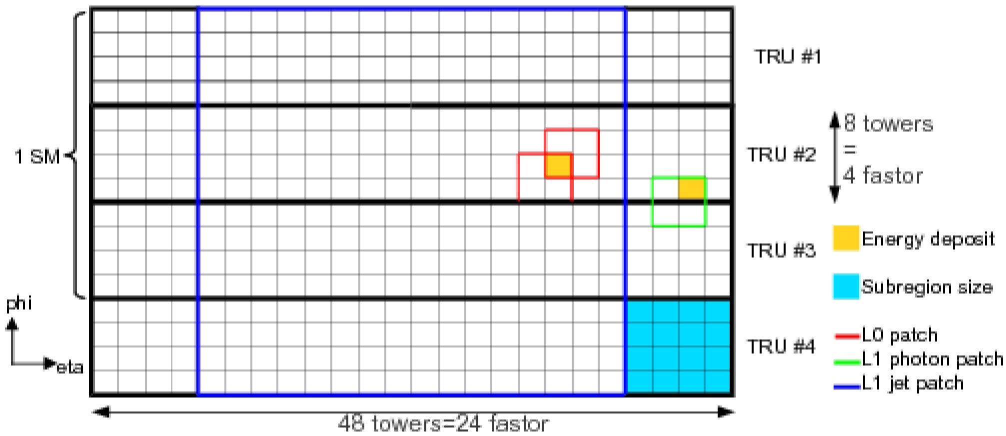

Figure 3.6.: Schematic view of the EMCal trigger system. [BACB+13]

4×24 modules (8×48 towers) and the analog signal sum over each module is called a *fastOR* unit. Four fastOR units (2×2) can be combined into a *patch*. For each trigger region, there is a corresponding Trigger Region Unit (TRU) that digitises the fastOR signals. This then computes the sum for each possible combination of fastORs into patches within the trigger region and compares it to a threshold. The local triggers of each TRU are collected in the Summary Trigger Unit (STU), which computes the final global L0 trigger. To set off the L0 trigger, at least one of the patches in any trigger region needs to exceed the threshold.

L1 Trigger

In the case of a positive L0 trigger, the TRU uses the stored signal information of the fastORs to compute the new patch combinations of the L1 trigger. The

L1 trigger is built to either identify high energy photons or jets. For the photon trigger (EGA), the patch size equals that of the L0 trigger with the difference that fastORs of adjacent trigger regions are allowed to form patches as well, which leads to a better trigger efficiency. The threshold of the EGA trigger is computed event by event (depending on multiplicity), relying on the input of the V0 detector. The L1 jet trigger (EJE) uses a patch of 16×16 fastORs that stretches over 4 TRUs and a correspondingly higher threshold. Both L1 triggers can be run with two different thresholds, leading to the triggers EG1, EG2, EJ1 and EJ2. [BACB+13] [M+17]

3.3.2. Clusterisation

As described above, the energy of photons and electrons is deposited in the EMCal cells (towers) via electromagnetic showers. The energy of such a shower spreads out and generates a signal in several EMCal cells. To identify an incoming photon with the EMCal detector, the single cell signals have to be combined into *clusters*, whose total signal corresponds to the energy of the measured photon. These clusters are formed by clusterisation algorithms. Cells with an energy higher than a certain threshold, E_{seed}, serve as clusterisation seeds. If such a cell is found, the adjacent cells will be added to the cluster if their energy exceeds a minimum energy threshold E_{min}. The cell with the highest energy serves as the first seed. There are two such clusterisation algorithms, the V1 and the V2 clusteriser, differing in their aggregation condition. The V1 clusteriser continues to add adjacent cells to the cluster, as long as each cell's energy exceeds E_{min}, while the V2 clusteriser additionally compares the energy of the adjacent cell candidate to the energy of the previously accepted cell, and only continues the aggregation if the new cell's energy is lower.

The two clusterisers can produce a very different outcome when it comes to *merged clusters* (overlapping clusters produced by two or more particles). An example of the different treatment is given in figure 3.7. In the case of a cell energy distribution with two local maxima, it can be seen that the V1 clusteriser forms one cluster containing the number of local maxima, while the V2 clusteriser results in two clusters with one local maximum each. As such, each clusteriser produces clusters with different properties in terms of energy distribution and shape. These properties can be constructive for certain types of analyses. [B+16b]

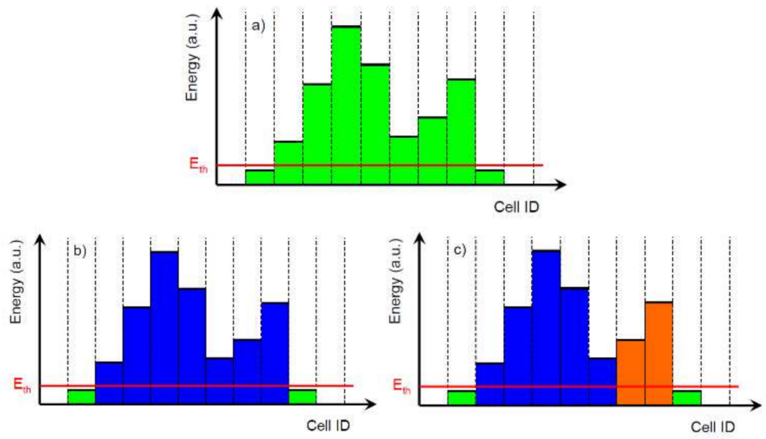

Figure 3.7.: Different outcome of clusteriser V1 and V2. a) Local cell energy distribution of adjacent cells in one dimension. b) The V1 clusteriser results in one cluster with two local maxima. c) The V2 clusteriser finds two clusters instead. [Col15]

4. Analysis Procedure

The aim of this thesis is to determine a raw prompt photon yield by applying an isolation cut, and subsequently to investigate its signal-to-background ratio. The second part will be achieved by using the two-photon decay channel of neutral pions in order to reconstruct the amount of isolated π^0 decay photons. The analysis should result in a minimum contamination rate for the isolated photon yield and hence could be taken as a measure for the effectiveness of the applied isolation cut. This chapter covers the exact analysis procedure including photon and π^0 meson selection criteria.

The photons in this analysis were detected by EMCal and for their reconstruction the clusteriser V2 was chosen. As previously mentioned, the V2 clusteriser splits up merged clusters with contributions from different particles, as long as each contribution causes its own local maximum within the cluster. While the two decay photons of a neutral pion in its rest frame could be observed back-to-back, the decay photons of a π^0 at high energies appear under the opening angle α due to the conservation of energy and momentum. The higher the π^0's energy, the smaller the angle α. In the EMCal this leads to overlapping clusters, as shown in figure 4.1.

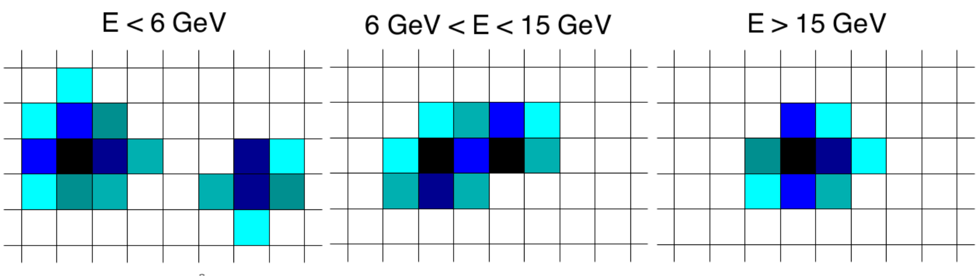

Figure 4.1.: Example of the cluster production in the EMCal by two incoming π^0 decay photons for different energy ranges of the meson. [B+16a]

By splitting the merged clusters with two local maxima, the V2 clusteriser resolves the decay photons up to a higher energy scale than the V1 would, and is therefore commonly used for π^0 reconstruction. However, from 15 GeV onward the V2 algorithm starts to struggle since the EMCal cell size limits the resolution of local maxima.

4.1. Selection of Prompt Photon Candidates

The clusters, formed by the clusterisation process, have different properties like shape, energy content and number of cells. The selection of photon candidates from all given clusters depends on these properties.

4.1.1. Event Selection

Before the photon candidates in each event can be determined, the event itself has to fulfil certain criteria. Events that can be traced back to beam-gas interaction or other forms of noise will be rejected by the *physics selection*. Furthermore, the z-component of the primary vertex is required to lie within the range of $|v_z| < 10\,\mathrm{cm}$. This ensures a uniform detector acceptance in η; it can also contribute to pile-up rejection. A typical distribution for the z-component before the vertex cut can be seen in figure 4.2. The cross section of prompt photon production is very small;

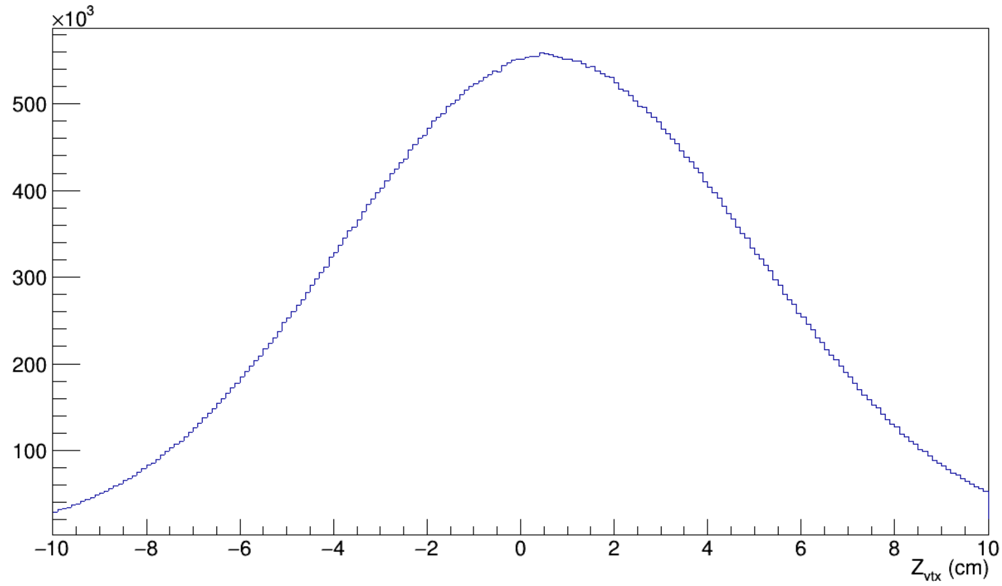

Figure 4.2.: Distribution of the z-component in different events (data taken from 2016k).

it is therefore unlikely to find and analyse corresponding events in data that were triggered by the V0AND. To increase the statistics for prompt photon production, the EMCal EGA trigger (described in section 3.3.1) is used to ensure that at least one high energy cluster has been detected by the EMCal. The exact trigger values change for different periods of data taking and are presented along with the used data sets.

4.1.2. Cluster Quality Cuts

To ensure that the analysed data is primarily a result of high energy collisions, *quality assurance studies* are performed at cell level for each data set. In this process, the EMCal cells are examined for dysfunctions and a *bad channel map* is created to exclude data from bad cells in analyses. Further measures to ensure cluster quality include the rejection of clusters that consist of only one cell (because these cells are most likely caused by particle interactions with the detector electronics) and the requirement of a minimum energy for a cluster due to a bad timing response of the EMCal for low energies. In this analysis, a value of $E_{\mathrm{min}} = 0.7\,\mathrm{GeV}$ is chosen. Due to the very small bunch spacing time of 25 ns during the data taken at $\sqrt{s} = 13\,\mathrm{TeV}$ in 2016, a timing cut will be applied to the clusters to dismiss clusters from different bunch crossings. The cluster time is defined by the time of measurement of its leading cell. The timing cut then allows a time window of $-12.5\,\mathrm{ns} < t_{\mathrm{clus}} < 13.0\,\mathrm{ns}$ around the measured current bunch crossing time.

4.1.3. Shower Shape Cut

An important criterion for identifying photons among the EMCal clusters is the cluster shape. An ellipsoidal parameterisation can be applied to the cluster by introducing the shower shape parameters σ^2_{long} and $\sigma^2_{\mathrm{short}}$, which can be seen as representative for the long and short axis of the shower surface ellipse. σ^2_{long} has been proven to be a good measure for photon identification. A single photon cluster tends to be rather circular and has a value of $\sigma^2_{\mathrm{long}} \approx 0.25$, while hadronic or merged clusters have broader or oval forms and result in larger values. [B+16b] Electrons, however, have a similar shape to photons and cannot be rejected by this method. Figure 4.3 shows the σ^2_{long} distribution before and after the application of the cluster cuts. A clear peak around $\sigma^2_{\mathrm{long}} \approx 0.25$ indicates the dominant

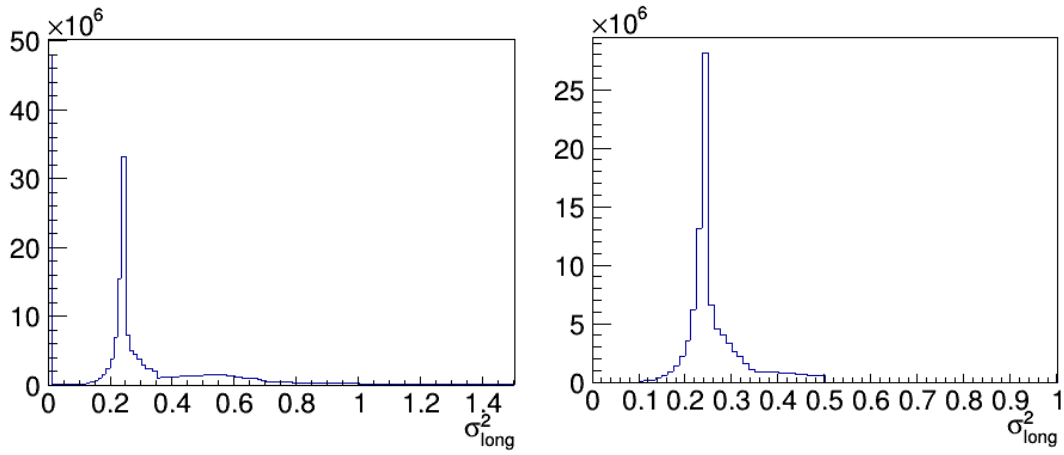

Figure 4.3.: σ^2_{long} distribution before (left) and after (right) the application of the cluster cuts (data from period LHC16k).

share of photons and electrons within the cluster yield. The contribution at higher σ^2_{long} values is comparatively small. This can be explained by the V2 clusterisation, which splits the clusters with multiple contributions that otherwise would have led to higher values of σ^2_{long}. The shape cut thus has more importance when using the V1 clusteriser. Nevertheless, there could be hadronic contributions left, as well as merged decay photons from highly energetic mesons with a small enough opening angle to result in only one local maximum. The higher the meson energy and the smaller the opening angle of a decay, the smaller the corresponding σ^2_{long} gets, approaching the value for photons. Hence, an energy dependent cut is applied, accepting values between $0.1 < \sigma^2_{\mathrm{long}} < 0.5$ for small energies and going down to $0.1 < \sigma^2_{\mathrm{long}} < 0.35$ for high energies.

4.1.4. Isolation Cut

As charged particles leave tracks in the ITS and TPC, both of which covering a larger pseudorapidity range than the EMCal ($|\eta| \leq 0.9$ vs. $|\eta| \leq 0.7$), the position of each EMCal cluster can be compared with extrapolated charged particle tracks. When a charged track matches with a cluster in the EMCal, that cluster is considered to be caused by the same charged particle and will be rejected.
This method strongly reduces the share of electrons and any remaining charged hadrons within the cluster sample, so that the primary contribution should come from single photons. On the other hand, a significant amount of photons convert in the detectors between the TPC and the EMCal. These conversions cannot be matched to a track and therefore stay part of the final photon sample. Depending on the opening angle, these electron-positron pairs will either result in one cluster so that the full energy of the photon can be automatically reconstructed, or two. The resulting impact on the analysis is discussed in further chapters. [Lod18]

In this analysis, the charged particle track matching will be included in the applied isolation criteria and therefore no further cut is necessary. As this thesis focuses on the effectiveness of the isolation cut rather than a final determination of a corrected prompt photon yield, the main analysis will be carried out for four different isolation radii ($R_{\mathrm{iso}} = 0.1, 0.2, 0.3, 0.4$). The hadronic activity will be determined by the total p_{T} of all charged particles measured within the cone. It is convenient to take the EMCal clusters into account as well, to get a more complete picture of the hadronic activity via decay photons. The inclusion of EMCal clusters, however, reduces the acceptance area for possible prompt photons, since the chosen cone around the photon candidate has to fully lie within the EMCal acceptance. At the convenient isolation radius of $R_{\mathrm{iso}} = 0.4$, this means a restriction to approximately 25 % of the EMCal acceptance. Using only charged particles for the calculation of the hadronic activity allows the area to expand up to 70 % of the EMCal acceptance, which enables a better statistic. However, not taking EMCal clusters into account might lead to a less pure prompt photon yield. The cut on the allowed energy in the cone has been chosen to be energy dependent, restricting the limit to 10 % of the photon candidate's energy. The isolation principle is depicted in figure 4.4.

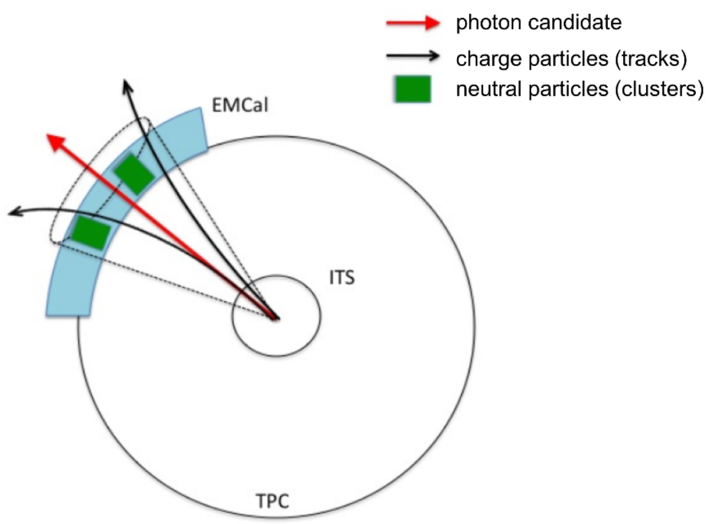

Figure 4.4.: Schematic view of an isolation cone around a photon candidate containing two charged particle tracks. [X+18]

In case a charged particle deposits energy in the EMCal and that cluster will be tested for isolation, the corresponding track will be inside the cone with an energy at least equal to that of the cluster. Subsequently, the cluster will be rejected.

4.1.5. Acceptance Cuts

The chosen acceptance cuts for this analysis come from the combination of ITS, TPC and EMCal acceptance ranges. The charged particles used for the isolation are measured within the pseudorapidity range of $|\eta| < 0.9$, but over the full azimuth. Hence, the largest used radius ($R_{\text{iso}} = 0.4$) restricts the employable area on the EMCal surface to a pseudorapidity range of $|\eta| < 0.5$, while the full range in ϕ can be exploited. Figure 4.5 displays the energy distribution for the full EMCal acceptance (left) and the area that is used in this analysis (right). A summary of

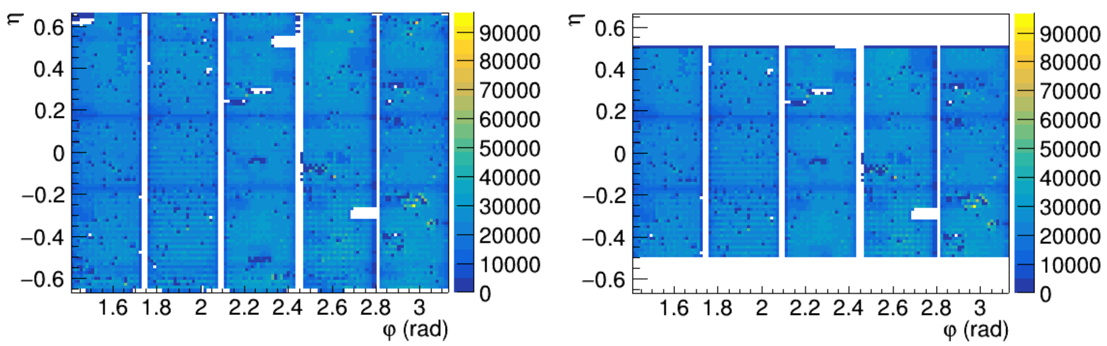

Figure 4.5.: Energy distribution for the full EMCal acceptance of five super modules (left) and used acceptance in η for this analysis due to the size of the biggest chosen isolation cone (right), (data from period LHC16k).

all applied cuts and parameters of the clusterisation process are displayed in table 4.1. The remaining clusters form the raw prompt photon yield. In the following section, the method for determining the fraction of π^0 decay photons within the measured prompt photon yield is presented.

Clusterisation Settings	
clusteriser	V2
seed cell energy	$E_{\text{seed}} > 0.5\,\text{GeV}$
minimum cell energy	$E_{\text{min}} > 0.1\,\text{GeV}$
Quality Cuts	
cluster time	$-12.5\,\text{ns} < t_{\text{clus}} < 13\,\text{ns}$
cluster energy	$E_{\text{clus}} > 0.7\,\text{GeV}$
minimum N_{cells}	≥ 2
Shape Cut	
shape parameter σ^2_{long}	$0.1 \leq \sigma^2_{\text{long}} \leq 0.5$
energy dependence	$\sigma^2_{\text{long,max}} = 0.32 + 0.0072 E^2_{\text{clus}}$
Isolation Cuts	
R_{iso}	0.1, 0.2, 0.3, 0.4
$p_{\text{T}}^{\text{thresh}}$ $(\epsilon p_{\text{T}}^{\gamma})$	$\epsilon = 0.1$
Acceptance Cuts	
longitudinal	$-0.5 \leq \eta \leq 0.5$
azimuthal	$1.4 \leq \phi \leq 3.15$

Table 4.1.: Summary of applied cluster cuts based on the EMCal meson analysis [M+17]

4.2. Invariant Mass Analysis

The largest share of decay photons that can possibly contaminate the prompt photon yield comes from π^0 decays into two photons. The two photons, however, conserve the invariant mass of the neutral pion, from which it is possible to reconstruct the meson. The invariant mass of a system of two photons is given by

$$M_{\gamma_1\gamma_2} = \sqrt{2E_{\gamma 1}E_{\gamma 2}(1 - \cos\theta_{12})} \tag{4.1}$$

where $E_{\gamma 1}$ and $E_{\gamma 2}$ are the energies of the decay photons and θ_{12} represents the opening angle between them. By pairing the photon candidates and calculating the invariant mass of the pairs, an invariant mass distribution can be obtained. An example of such a distribution is given in figure 4.6. Two peaks are noticeable within a continuous spectrum. The left peak is positioned at $M_{\gamma_1\gamma_2} \approx 0.13\,\text{GeV/c}^2$, which corresponds to the invariant mass of the neutral pion $(0.135\,\text{GeV/c}^2)$, while the peak on the right is caused by the decay of the η meson $(0.548\,\text{GeV/c}^2)$ that has a two-photon decay channel as well. The continuous spectrum is a result of the combination of uncorrelated photons. Subtracting this continuous background

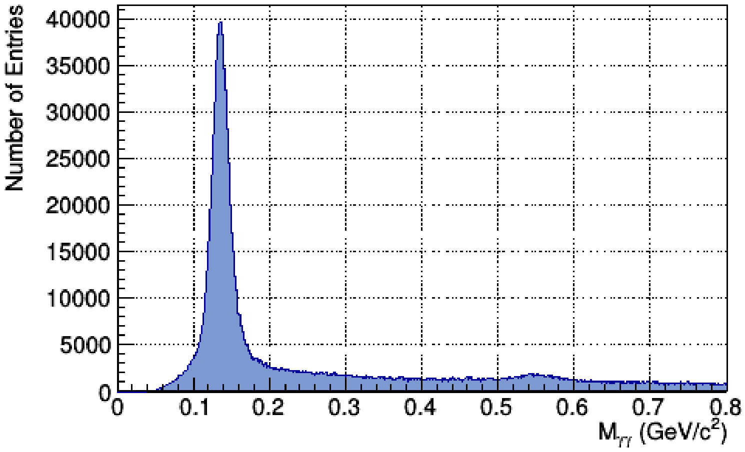

Figure 4.6.: Exemplary invariant mass distribution for the pairing of photon candidates within a certain energy range (data taken from LHC16k).

and integrating the remaining peaks could lead to the number of π^0, η or decay photon candidates, dependent on the condition under which the distribution was constructed. The exact procedure for determining isolated decay photons based on the invariant mass method is described in the following section. The procedure is based strongly on the EMCal meson analysis that can be found in [M$^+$17], with a few variations due to the different aim of measuring decay photons instead of mesons.

4.2.1. Isolated π^0 Decay Photons

In this thesis, the p_T-dependent yield of π^0 decay photons shall be determined as a subfraction of the measured isolated photon yield. Because there is a possibility that one of two decay photons has been isolated and not the other, it is necessary to combine the isolated photons with a pool of photon candidates in pre-isolation state. The exact procedure can be outlined as follows. In every event, the cluster candidates that pass all cuts apart from the isolation will be stored in a pool for general photon candidates. Afterwards, the isolation cut will be applied and the fraction of photon candidates that pass will be stored in a pool for isolated photon candidates. Every isolated photon candidate will then be paired with every other photon from the general photon candidate pool. In case a pair of candidates passes specific meson criteria (which is covered in section 4.2.3), the calculated invariant mass of the pair and the p_T of the corresponding isolated photon is added to a 2-dimensional histogram as shown in figure 4.7. The dominant contribution around the invariant mass of the π^0 can be seen once again. The large white space at the bottom goes up until 0.7 GeV/c and corresponds to the minimum energy cut for the clusters. This histogram can be evaluated for reasonable p_T ranges, so called *p_T-bins*. Each bin then contains a corresponding invariant mass distribution, similar to that in figure 4.6. The more bins the histogram is divided into, the better the resolution of the resulting decay photon yield, but the worse the statistics for each

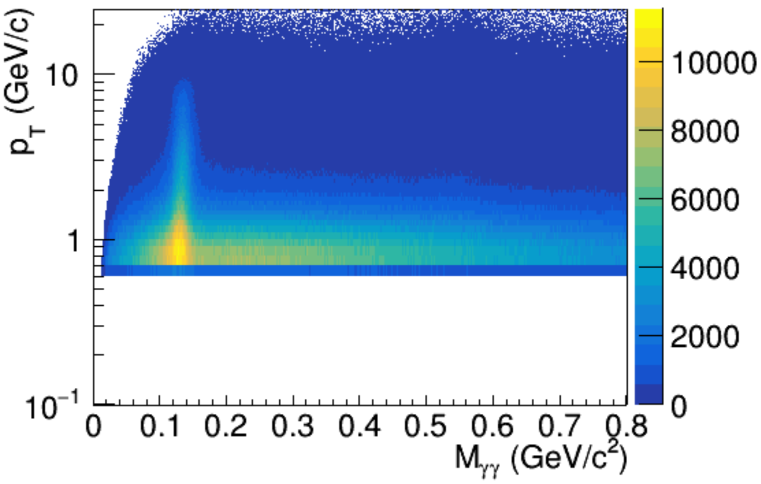

Figure 4.7.: p_{T}-dependent invariant mass distribution for decay photon analysis (data taken from LHC16k).

bin. As such, a compromise has to be made between both. The chosen p_{T}-bins are displayed in table 4.2. To extract the yield of π^0 decay photons for each p_{T}-bin,

p_{T}-bins (GeV/c)			
1:	$7.0 < p_{\mathrm{T}} < 7.25$	11:	$9.5 < p_{\mathrm{T}} < 10.0$
2:	$7.25 < p_{\mathrm{T}} < 7.50$	12:	$10.0 < p_{\mathrm{T}} < 10.5$
3:	$7.5 < p_{\mathrm{T}} < 7.75$	13:	$10.5 < p_{\mathrm{T}} < 11.0$
4:	$7.75 < p_{\mathrm{T}} < 8.0$	14:	$11.0 < p_{\mathrm{T}} < 12.5$
5:	$8.0 < p_{\mathrm{T}} < 8.25$	15:	$12.0 < p_{\mathrm{T}} < 13.0$
6:	$8.25 < p_{\mathrm{T}} < 8.5$	16:	$13.0 < p_{\mathrm{T}} < 14.0$
7:	$8.5 < p_{\mathrm{T}} < 8.75$	17:	$14.0 < p_{\mathrm{T}} < 15.0$
8:	$8.75 < p_{\mathrm{T}} < 9.0$	18:	$15.0 < p_{\mathrm{T}} < 17.0$
9:	$9.0 < p_{\mathrm{T}} < 9.25$	19:	$17.0 < p_{\mathrm{T}} < 21.0$
10:	$9.25 < p_{\mathrm{T}} < 9.5$		

Table 4.2.: Chosen p_{T}-bins for the extraction of π^0 decay photon yields from the 2D invariant mass histogram.

first the background has to be determined and subtracted, then the remaining signal can be integrated. Due to the combinatorial character of the background, a common method for its estimation is the *event mixing* method.

4.2.2. Event Mixing

As the name suggests, the event mixing method pairs the photons of different events to avoid any correlation between two decay photons. The produced background shape, however, has been found to depend on primary v_{z}-position and particle multiplicity. Therefore, events are sorted into different bins for both quantities, and photons from different events only get mixed if both events show similar properties in terms of multiplicity or v_z-position. In this analysis, the events are stored photon multiplicity dependent, since that has been proven as the most accurate background description so far. The event mixing method determines the shape of the background, but not the scale. The background will be normalised to the invariant mass distribution, either on the left or on the right side of the peak. Figure 4.8 displays the invariant mass distributions in the range of the π^0 for the p_T-bins from table 4.2. The lower p_T-bins show very little background, but

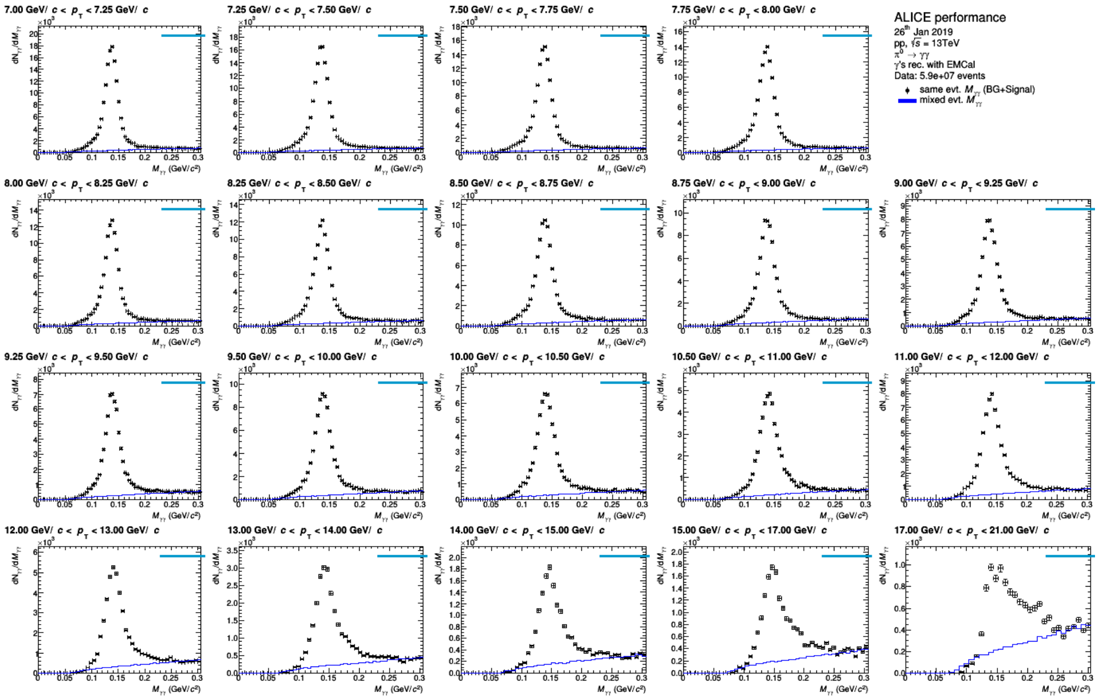

Figure 4.8.: Invariant mass distributions for all chosen p_T-bins at $R_{iso} = 0.1$. The scaled mixed event background can be seen as a blue line (data taken from LHC16k).

an increase is visible, indicating the impact of merged clusters at higher p_T.

4.2.3. Meson Cuts

The general criteria that the calculated π^0 candidate has to fulfil are displayed in table 4.3.

Meson Cuts	
energy asymmetry α	$0 \leq \alpha \leq 1$
opening angle θ	$\theta = 17\,\text{mrad} + 1$ cell distance
rapidity y	$\lvert y \rvert < 0.8$

Table 4.3.: Summary of applied meson cuts based on the EMCal meson analysis. [M+17]

The energy asymmetry is given by

$$\alpha = \frac{E_{\gamma 1} - E_{\gamma 2}}{E_{\gamma 1} + E_{\gamma 2}}, \tag{4.2}$$

with $E_{\gamma 1}$ and $E_{\gamma 2}$ representing the energies of the decay photons and, as its name suggests, it measures the decay asymmetry. $\alpha = 0$ would represent a purely symmetric decay where the energy is split up equally between the two decay photons, while $\alpha = 1$ would be the limit where one photon goes straight to the EMCal and the other into the opposite direction[7]. The most symmetric decay also corresponds to the smallest opening angle. In this analysis, the whole spectrum of decays will be taken into account. As previously mentioned, the resolution of two decay photons with a very small opening angle within one event is restricted by the EMCal cell size, so that π^0 mesons with $p_{\mathrm{T}} > 20\,\mathrm{GeV/c}$ will appear as one cluster and the invariant mass method will not work. In mixed events, however, there is no such restriction. Hence, a minimum opening angle has to be chosen that provides a comparable distribution. $\theta = 17\,\mathrm{mrad}$ has been proven to be the best cut value, together with the additional criterion that two leading cluster cells cannot be adjacent. The cut on the mesons rapidity is due to the restricted acceptance of the EMCal detector.

4.2.4. Signal Extraction

The final signal extraction works by fitting the invariant mass distributions for each p_{T}-bin from table 4.2 with a Gaussian function, after the mixed event background has been subtracted. The multiple fitted spectra can be seen in figure 4.9, and figure 4.10 depicts a magnification of the distribution with fit for $9.2\,\mathrm{GeV} < p_{\mathrm{T}} < 9.5\,\mathrm{GeV}$. The left side of the fit describes an exponential fall off, which is implemented into the fit function to include the contribution of conversion electrons and positrons. In order to account for a remaining background that the event mixing method did not cover, the function also consists of a linear part. The fit is used to determine the invariant mass position M_{π^0}; the standard integration window is chosen to be $[M_{\pi^0} - 0.05, M_{\pi^0} + 0.04]$ and can be seen around the peaks in figure 4.9 as solid lines. A wider and a narrower integration window are usually chosen to estimate errors. The actual π^0 decay photon yield will then be determined by adding the yields of the bins within the integration window. It is noticeable that, at the right side of the peak, the displayed invariant mass distributions are not very well described by the standard Gaussian fit. This is because the fit function has been worked out for 8 TeV data. Since several features changed for the data taken at 13 TeV (eg. bunch spacing and energy), the fit function needs to be revised in order to properly converge for 13 TeV data. In this analysis there was no scope for an adjustment, thus standard settings have been used to get a first impression of the application of the invariant mass analysis on isolated photons. The extracted yields for the different isolation radii for the same data set can be seen in figure 4.11.

[7] Because it travels at the speed of light, it would not reach the detector.

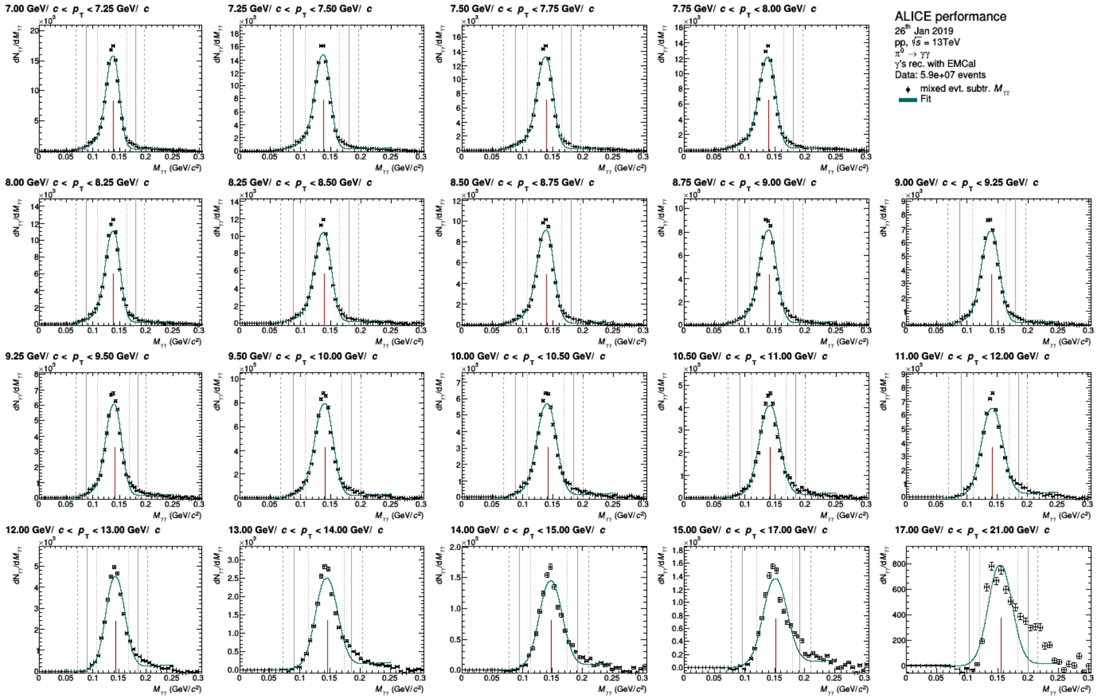

Figure 4.9.: Invariant mass distribution with subtracted background and fit with $R_{\mathrm{iso}} = 0.1$ (data taken from LHC16k).

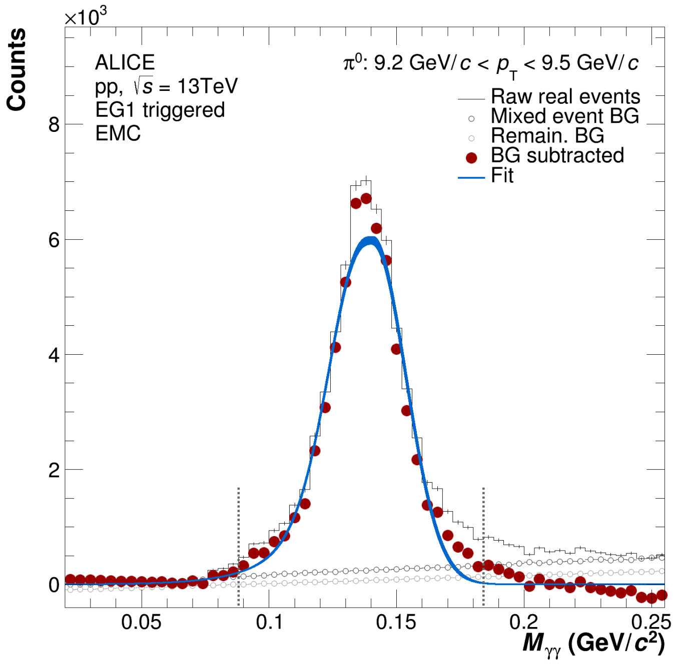

Figure 4.10.: Invariant mass distributions with subtracted background and Gausian fit for and $R_{\mathrm{iso}} = 0.1$ (data taken from LHC16k).

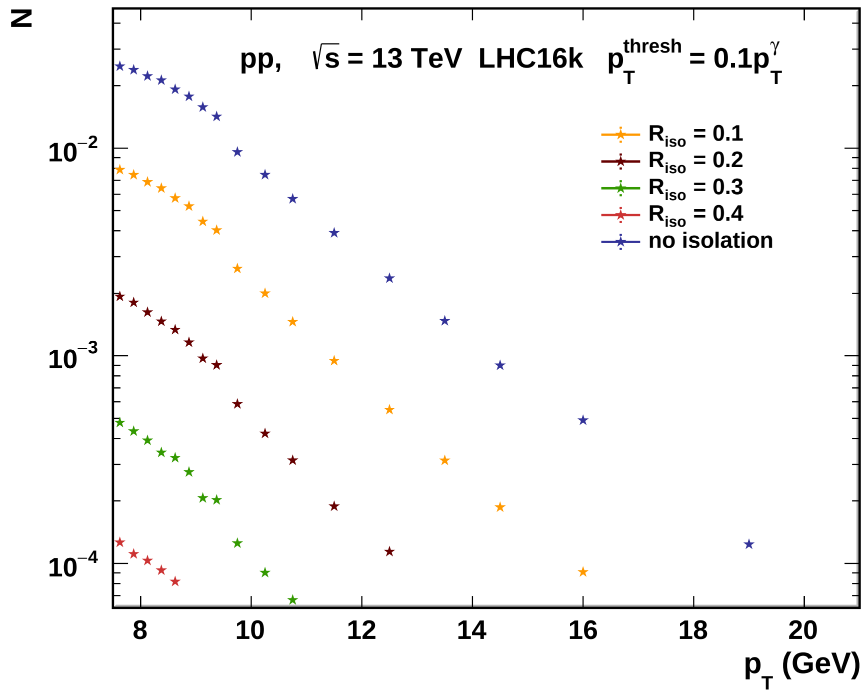

Figure 4.11.: p_{T}-dependent invariant mass distribution for decay photon analysis (data taken from LHC16k).

5. Monte Carlo Studies

Before applying the introduced approach for estimating the contamination of the raw isolated photon yield to a data set, an evaluation will be done based on simulated data. In the simulation, results of pp collisions are generated by *Pythia 8*. Pythia is a Monte Carlo (MC) event generator that is based on the generation of random numbers in order to reproduce a huge number of possible event outcomes. An event is divided into subprocesses that are simulated one after another. The initial hard scattering and parton shower are derived from perturbative QCD; the hadronisation uses phenomenological models that are based on the QCD potential. The underlying event is considered as well. The different theories and models leave scope for improvement in the form of tunable parameters that can be determined by comparison with data. [SMS06]
As it is impossible to analyse the amount of data from high energy collisions without making assumptions about the underlying processes leading to a final measurable yield, simulation and experiment are very intertwined in high energy physics and it is difficult for one to be used or improved without the other. However, Pythia only generates the events itself, so that further processing is required in order to make the outcome comparable with measured data. Therefore, the interaction of final state particles with the ALICE detector has been simulated with *Geant* 3.

Monte Carlo data sets store information about the particle's type and origin. These can be used to get insight into particle responses to given analysis methods within the limit of the theories and models that the simulation is based upon. A set of such MC data is used in this chapter to evaluate the chosen isolation criteria by looking at their efficiency in selecting the given prompt photons, as well as their ability to reject cluster candidates coming from other sources. Furthermore, the previously introduced invariant mass method shall be used and assessed on a Monte Carlo level.

5.1. Monte Carlo Data Sets

For prompt photon studies, two types of MC data sets are relevant: one for the description of the prompt photon signal and one for the background processes. For the signal, only events that produced a prompt photon during the initial hard scattering are taken into account; this set is called gamma-jet (γ-jet) MC. The corresponding background MC was simulated under the condition of producing two back-to-back parton jets, and is called jet-jet MC. The chosen MC productions simulate pp collisions at $\sqrt{s} = 13\,\text{TeV}$, and fulfil the additional criterion that the prompt photon (γ-jet) or a decay photon with at least $7\,\text{GeV}$ (jet-jet) were produced in the EMCal direction. The two sets have been produced in 2017 and are called LHC17i3a1 (γ-jet) and LHC17i3c1 (jet-jet). More detailed information can be found on the JIRA website [Web17].

As the cross section strongly decreases with higher momentum transfer Q^2 in the initial hard scattering, the statistic for particle yields at high p_T would be far worse than at low p_T. In Monte Carlo productions, this difference can be balanced out by generating events in p_T^hard-*bins* that correspond to a certain range of Q^2. For each p_T^hard-bin, the same number of events will be generated. This process alone would result in unrealistically high yields for high p_T particles in comparison to the low p_T range. Therefore, the corresponding average cross section is calculated by Pythia for each p_T^hard-bin, which can be used to determine associated weights ω in order to obtain a normalised p_T-spectrum. The weight is given by

$$\omega = \frac{\bar{\sigma}_\text{evt}}{\sum\limits_\text{evt} N_\text{trials}} N_\text{evt}, \tag{5.1}$$

where $\bar{\sigma}_\text{evt}$ is the cross section the events from a given p_T^hard-bin correspond to on average, N_trials represents the number of trials before the production of the desired conditions, and N_evt the total number of accepted events. The p_T^hard-bins the two MC sets were produced in are listed in table 5.1, and figure 5.1 displays the unweighted yield (left) and the weighted cross section (right) for the γ-jet MC.

p_T^hard-bins (GeV/c)			
jet-jet		**γ-jet**	
1:	$8 < p_\text{T}^\text{hard} < 10$	1:	$5 < p_\text{T}^\text{hard} < 11$
2:	$10 < p_\text{T}^\text{hard} < 14$	2:	$11 < p_\text{T}^\text{hard} < 21$
3:	$14 < p_\text{T}^\text{hard} < 19$	3:	$21 < p_\text{T}^\text{hard} < 36$
4:	$19 < p_\text{T}^\text{hard} < 26$	4:	$36 < p_\text{T}^\text{hard} < 57$
5:	$26 < p_\text{T}^\text{hard} < 35$	5:	$57 < p_\text{T}^\text{hard} < 84$
6:	$35 < p_\text{T}^\text{hard} < 48$	6:	$84 < p_\text{T}^\text{hard}$
7:	$48 < p_\text{T}^\text{hard} < 66$		
8:	$66 < p_\text{T}^\text{hard}$		

Table 5.1.: p_T^hard-bins for γ-jet and jet-jet MC productions.

5.2. Prompt Photon Isolation Efficiency

The isolation *efficiency* is defined as the ratio of all validated isolated prompt photons $\gamma_\text{iso}^\text{prompt}$ to all true prompt photons $\gamma_\text{all}^\text{prompt}$ that passed the general photon cuts, apart from the isolation:

$$\epsilon_\text{iso} = \frac{\gamma_\text{iso}^\text{prompt} / dp_\text{T} d\eta}{\gamma_\text{all}^\text{prompt} / dp_\text{T} d\eta}. \tag{5.2}$$

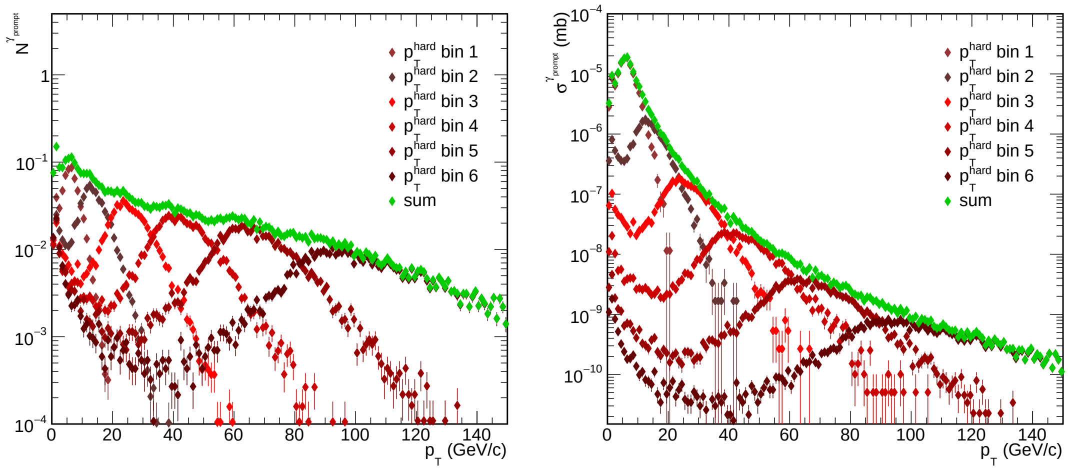

Figure 5.1.: $p_{\mathrm{T}}^{\mathrm{hard}}$-bin contribution unweighted (left) and weighted (right) for the γ-jet MC data.

Due to photon conversions in front of the EMCal, the prompt photon signal consists of clusters caused by unconverted photons (50.1 %) and clusters caused by conversion products (49.9 %). The efficiency has been determined for both cases using the γ-jet Monte Carlo production as input. The results can be seen in figure 5.2 for the unconverted and in figure 5.4 for the converted case.

5.2.1. Unconverted Prompt Photons

The first thing to notice is the increase of ϵ_{iso} with higher p_{T}: more prompt photons are selected by the isolation criteria at higher momentum range. This could be explained by the p_{T}-dependent threshold that allows more uncorrelated tracks (from the underlying event) within the cone for higher energies of the prompt photon. This assumption would be easy to check by changing the isolation energy cut to a fixed value and comparing the results. At the smallest isolation radius of $R_{\mathrm{iso}} = 0.1$, ϵ_{iso} approaches 1; for larger radii the curve is shifted towards lower ϵ_{iso}, because the criteria gets tighter and more susceptible to possible background from the underlying event. The behaviour between 0 GeV and 10 GeV can be seen as an unphysical artifact of the production process of the γ-jet MC in $p_{\mathrm{T}}^{\mathrm{hard}}$-bins. The first bin starts at 5 GeV and all entries with lower p_{T} are the sum of low-energy tails of the spectra produced in each $p_{\mathrm{T}}^{\mathrm{hard}}$-bin. As a result, the low p_{T} range is not representative for the real prompt photon efficiency and will be omitted in this analysis. The yields for both cases (converted and unconverted prompt photons) and their behaviour for low p_{T} can be seen in figure 5.3. Using only charged particles for the estimation of hadronic activity leads to less strict criteria, hence enhancing the efficiency but at the same time reducing the rejection of background clusters in comparison to an energy threshold that accounts for neutral clusters. The advantages and disadvantages of each method could be subject to a more extensive study.

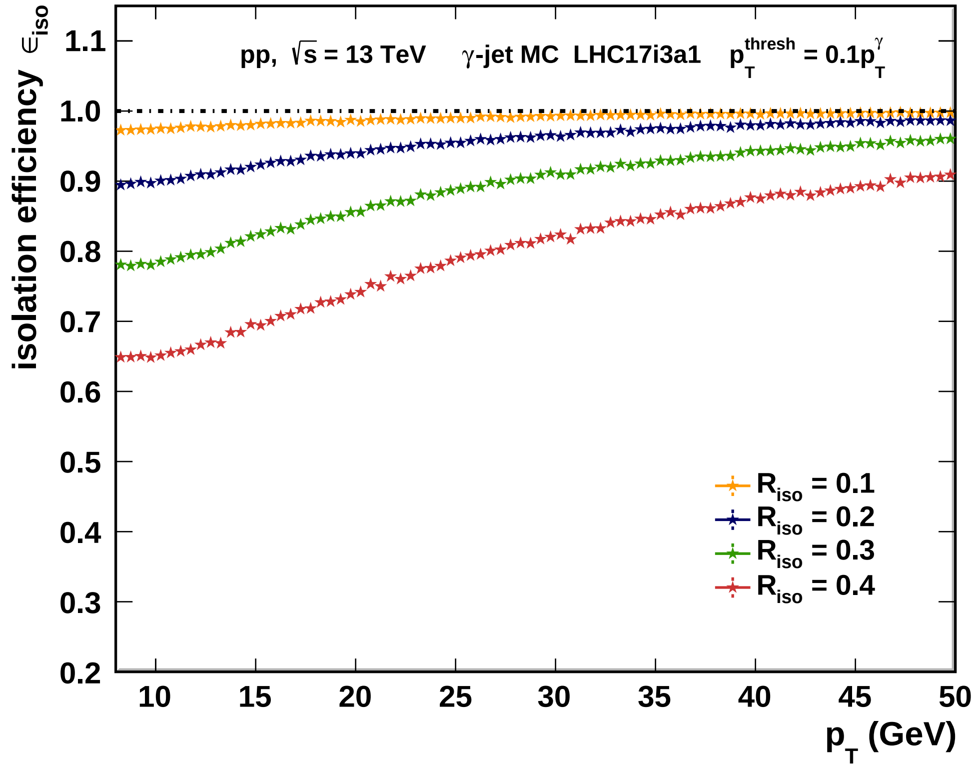

Figure 5.2.: Isolation efficiency for unconverted prompt photons.

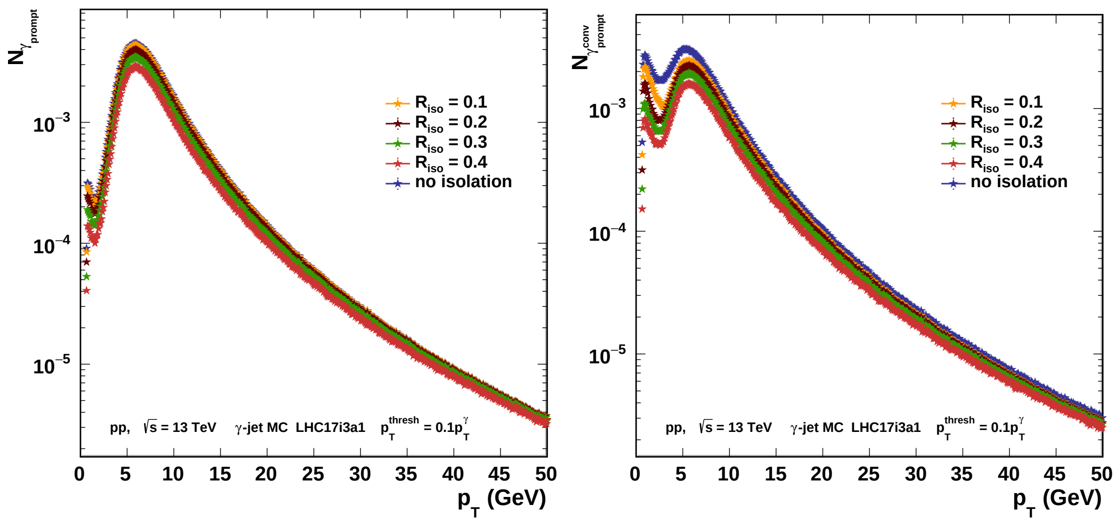

Figure 5.3.: Prompt photon yields for unconverted (left) and converted (right) prompt photons.

5.2.2. Converted Prompt Photons

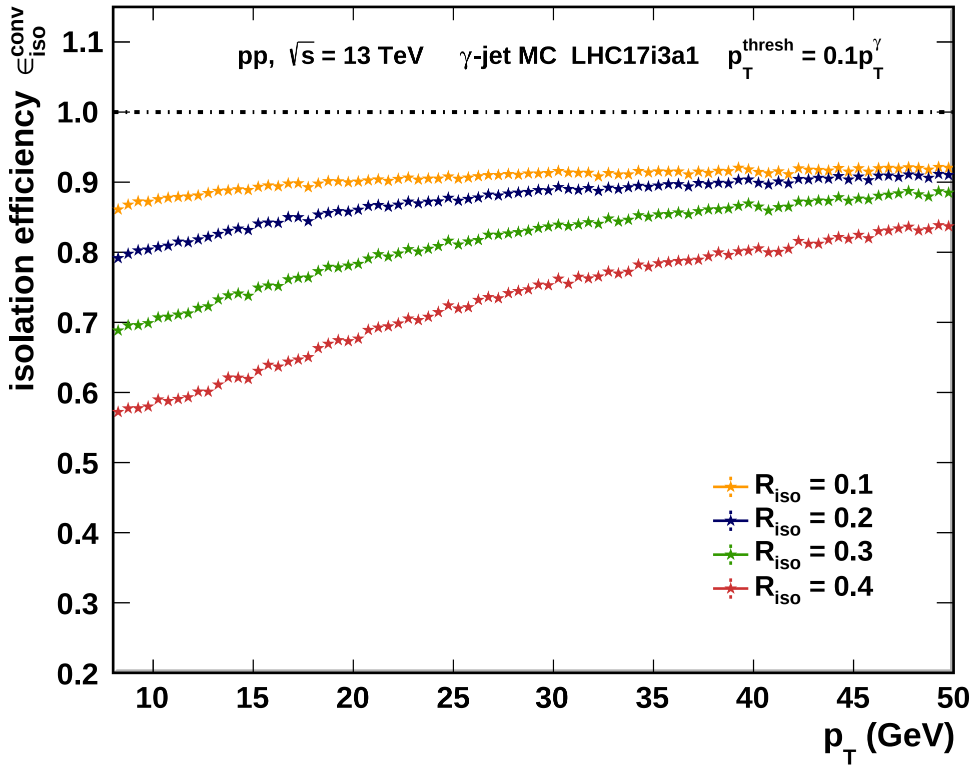

Figure 5.4.: Isolation efficiency for converted prompt photons.

Figure 5.4 shows the isolation efficiency for conversion electrons and positrons whose mother was found to be a prompt photon. There are is one main difference to figure 5.2. All curves appear to be shifted towards lower efficiencies. If a conversion occurs within the range of the TPC, a track can be reconstructed and the corresponding cluster will be rejected by the isolation criterion. As aforementioned, a large part of the conversions happen behind the TPC and therefore cannot be rejected by track matching. Based on that, the isolation efficiency shift could be related to the share of conversions that happen within the reconstruction range of the TPC and therefore not pass the isolation cut. According to the Monte Carlo simulation, converted prompt photons constitute nearly half of the extractable prompt photon yield, but only about 2 % of the converted photons have been double counted due to electron and positron depositing their energy separately. This could mean that most of the conversion pairs are measured as one cluster (due to a very small opening angle of the $e^+ - e^-$ pair) and therefore the shift towards lower energies due to conversions would not cause a large deviation. In order to make final conclusions about a possible energy shift, more detailed MC studies needed to be performed.

In order to assess the obtained efficiency results for the different isolation radii it is necessary to perform a similar study for background clusters.

5.3. Background Rejection Ability

The jet-jet MC has been used to apply the isolation criteria on a pure background sample that mainly consists of decay photons. Figure 5.5 depicts the share of these clusters that pass the isolation criteria. A clear dependence of the ratio on the isolation radius can be seen. The high efficiency of an isolation criterion with $R_{\text{iso}} = 0.1$, on the one hand entails a large acceptance of background clusters and, therefore, a weak signal-to-noise ratio (*purity*) on the other. The larger the

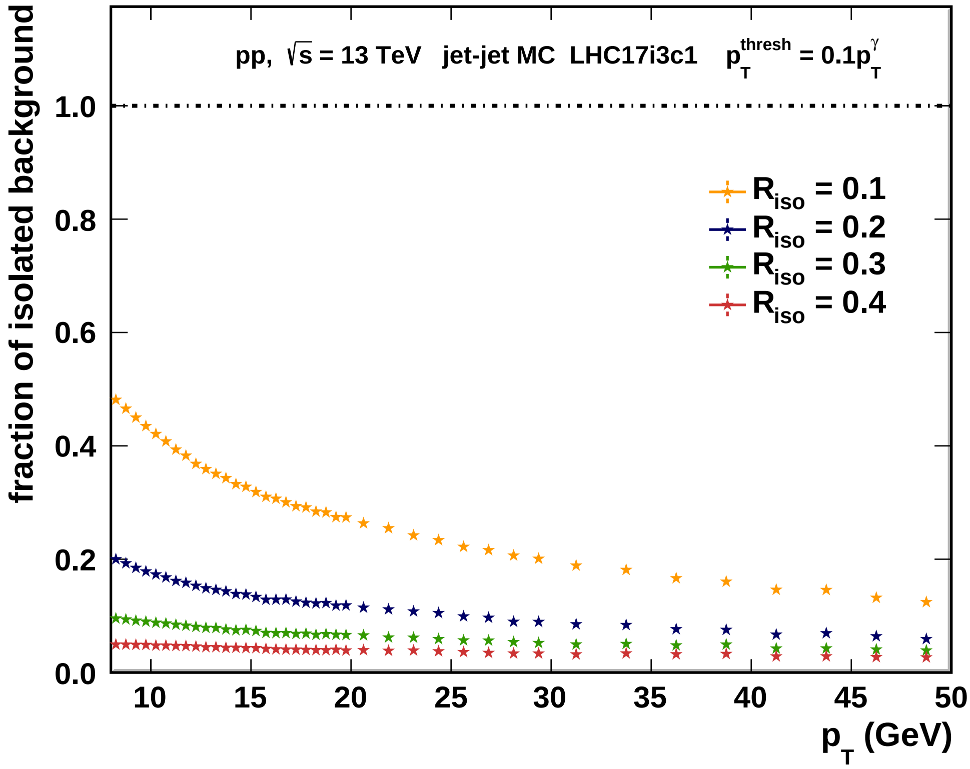

Figure 5.5.: Ratio of background clusters that pass the isolation cut.

radius, the better the rejection ability becomes: for $R_{\text{iso}} = 0.4$ only 5 % of the background clusters pass the criterion. The amount of accepted clusters seems to double (approximately) for a decrease of the radius by 0.1. Therefore, the change from $R_{\text{iso}} = 0.4$ to $R_{\text{iso}} = 0.3$, at about 10 GeV, only reduces the background rejection ability by 5 %, while the change from $R_{\text{iso}} = 0.2$ to $R_{\text{iso}} = 0.1$ causes a decrease of 20 %. The rejection generally improves with larger cluster p_{T}, which can be related to the jets getting narrower, and involved particles getting closer together with higher parton energies, thus leaving less room for isolated particles within the jets.

In conclusion, a good background rejection goes along with losing signal and statistics (also due to detector size, as mentioned in section 4.1.5). An effective isolation cut should therefore exhibit a good compromise between sufficient statistics and a high purity. The smallest radius, $R_{\text{iso}} = 0.1$, would result in

a low purity since, despite the use of triggered data, the background is still large. $R_{\text{iso}} = 0.3$ and $R_{\text{iso}} = 0.4$ both seem to provide reasonable performances in suppressing decay photons. An isolation cone with $R_{\text{iso}} = 0.4$ can provide a higher purity but removes a bigger share of the existing prompt photons, while an isolation cone with $R_{\text{iso}} = 0.3$ would provide a higher efficiency and more statistics but lower purity.
So far, the impact of the different isolation criteria on signal and background has been looked at separately and, as such, purity predictions for the different radii could only be made based on additional information about the pre-isolation signal share. Using the invariant mass method, in order to measure the decay photon yield as part of the raw isolated photon spectrum could provide a data driven method for purity determination.

5.4. π^0-Decay Photon Yield

In this section, the results of decay photon yields are determined via the invariant mass method and by using Monte Carlo production information. All yields are divided by the total cluster yields and thus display the relative contribution within each cluster yield. All ratios are displayed for the four isolation radii and additionally for the inclusive yield as a comparison.

5.4.1. Validation of the Invariant Mass Method

The relative share of π^0 decay photons for the different isolation radii, obtained through invariant mass reconstruction, can be seen in figure 5.6. In principle, the plot imitates the minimum contamination rate that shall be determined for data in the next chapter but, because of the lack of prompt photons in the jet-jet simulation, it simply shows the share of reconstructible decay photons. However, it still gives an impression of the reconstruction efficiency for π^0 decay photons, and it can be compared to true MC output in order to validate the invariant mass method itself. The corresponding invariant mass plots (involving the normalised mixed event background and the fitted results after subtraction) for all p_{T}-bins can be found in appendix A.1.

The ratios show several distinctive feature. For once, the share of reconstructible π^0 decay photons decreases strongly towards high p_{T}, which reveals the resolution limit of merged clusters in the EMCal. Furthermore, the curves all display a jump at about 10 GeV that could either be an effect of the imitated 7 GeV photon trigger or indicate a mistake/unreliability within the applied procedure. The ratio also shows a dependence on the isolation radius, which could mean that the different cluster types within the jet-jet MC sample respond differently to the applied isolation and, as a result, the share of π^0 decay photons could decrease. Another possibility could be a decreasing reconstruction efficiency with larger radii due to a lack of statistics. In order to evaluate these assumptions, the same ratio

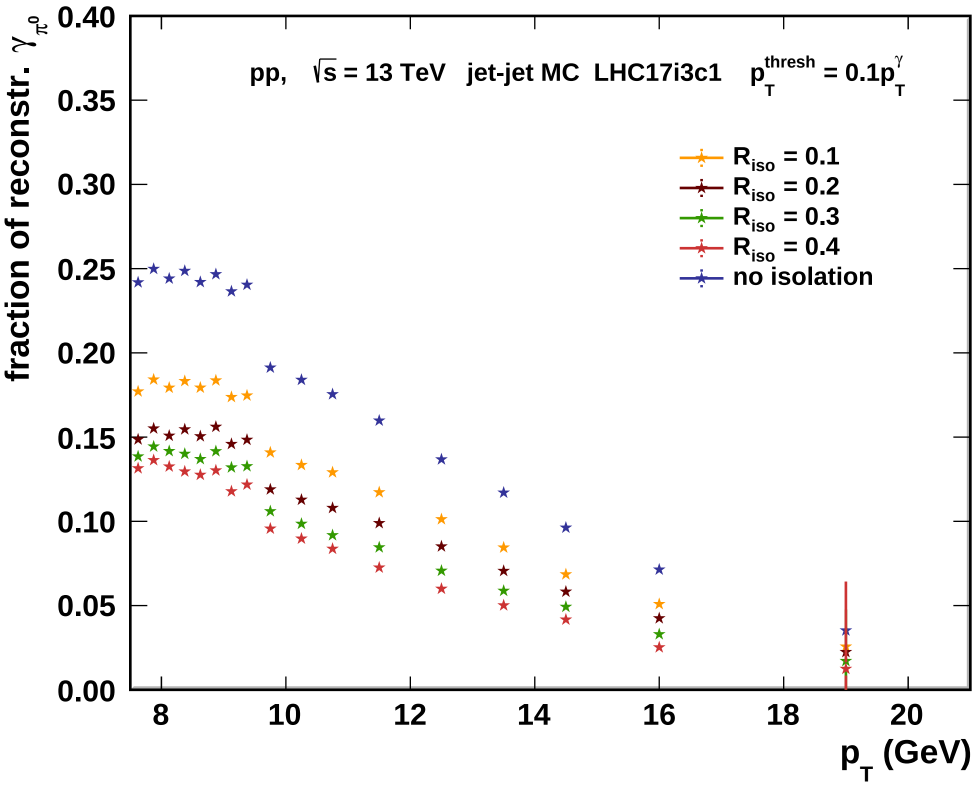

Figure 5.6.: Share of π^0 decay photons determined by the invariant mass method within the isolated cluster yield for different isolation cones.

has been plotted (figure 5.7) for cluster pairs that passed the meson cuts and that additionally have proven to be true photons coming from the same π^0. The converted photons have been included since they contribute to the invariant mass peak and are therefore part of the signal extraction. Overall, the ratios compare well apart from a few significant distinctions. Firstly, the jump does not appear in this plot, which indicates an issue with the invariant mass method and discards the trigger argument. Secondly, the ratio that has been obtained for the case of no applied isolation (at high p_T), is distinctively higher than the other curves in this plot. Since the jump happens in the same place for all five curves it looks very much like a binning issue, and also because it occurs precisely at the transition of one bin width to the next. Nevertheless, it does not seem to occur for the other bin width changes at higher p_T. At this point it is important to remember the fit function that did not converge very well on the right side of the invariant mass peaks. As such, displacements of the invariant mass positions of the π^0 and thus shifted integration windows may have occurred, which could entail a high uncertainty for the single yields in each p_T-bin. There would be no reason, however, for such effects to be exposed so distinctively in one place. Rather, it could cause a systematic shift or at least show a more continuous impact on the yield.

From 10 GeV onwards, the ratios for the isolated yields agree relatively well, considering the bias of the fit function and the strange jump at the start. Looking at the invariant mass plots shown in appendix A.1, the fits seem to converge

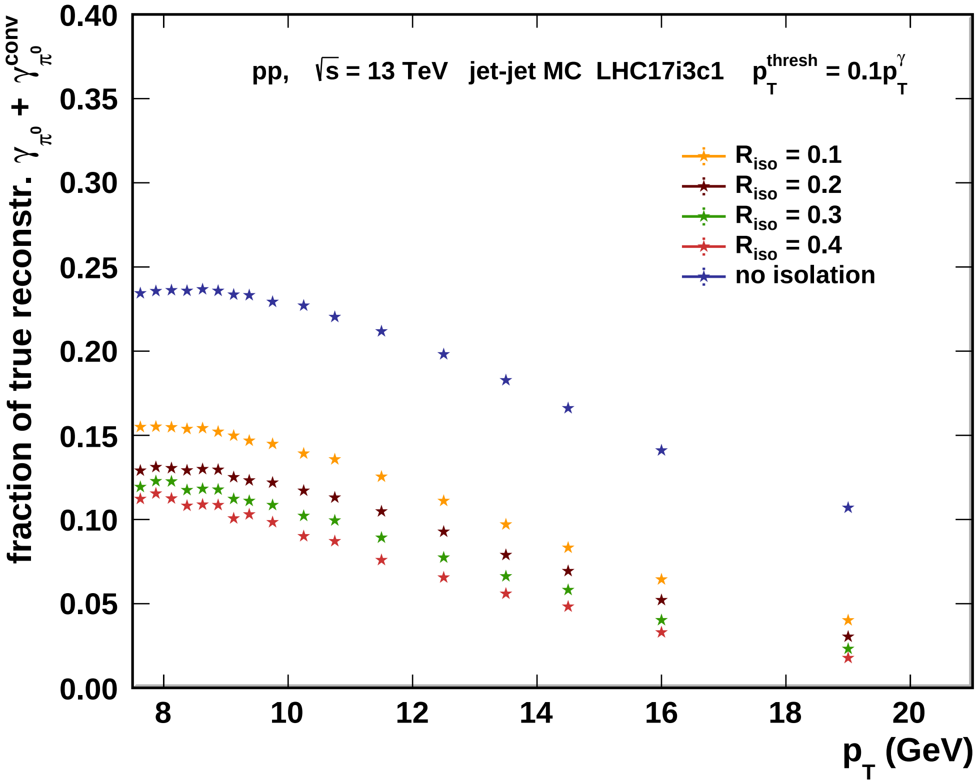

Figure 5.7.: Share of MC validated isolated π^0 decay photons that, combined with another photon, passed the meson cuts (conversions included).

better for isolated photon yields. Thus, the deviation of the curve for the inclusive photons (as opposed to isolated ones) might be based on a worse reconstruction efficiency, due to a larger background of charged particles. The radius dependence can be observed in the true MC output as well and thus indicates the presence of a particle that are easier isolated than the π^0 decay photons are. A decreasing reconstruction efficiency therefore might not be the reason for the separation, especially because the fits have been found to better describe the isolated invariant mass distributions.

In the following section, the total contribution of true π^0 decay photons to the background sample is presented in order to estimate the reconstruction efficiency of the invariant mass method.

5.4.2. True π^0 Decay Photons

The yield of all photon candidates, whose mothers were found to be neutral pions (true π^0 decay photons), is divided by the total yield of clusters for each isolation criteria and the inclusive spectrum. The results are displayed in figure 5.8. Dependent on the isolation criterion, the true share of π^0 decay photons within every cluster sample varies from 75 % up to 83 %. Especially at low p_T, this ratio also shows a weak dependence on the isolation radius. Noticeable here

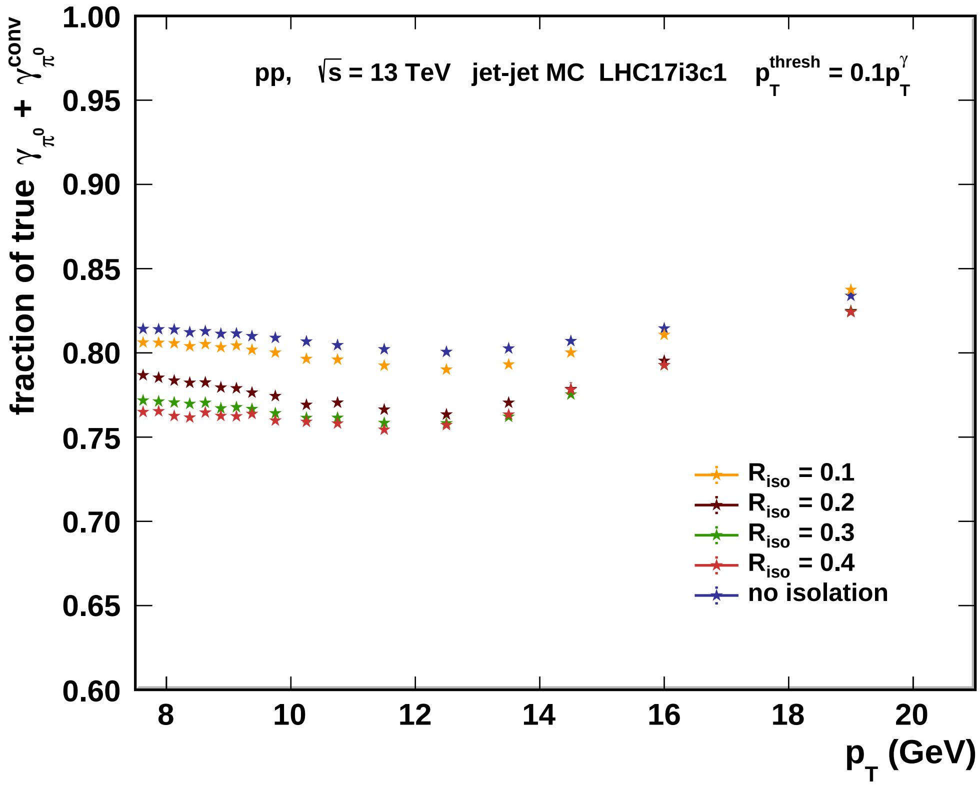

Figure 5.8.: Share of true π^0 decay photons within isolated cluster yield for different isolation cones (conversions included).

is the wide gap between the ratios at $R_{\text{iso}} = 0.1$ and $R_{\text{iso}} = 0.2$, suggesting that the result of an isolation with $R_{\text{iso}} = 0.1$ is closer to the inclusive spectrum than to that of the other isolation criteria. However, it is possible that the inclusive curve results in a lower share relative to the isolated ones due to charged particle contributions in the denominator. Compared to the former results, one can extract a reconstruction efficiency (at $p_{\text{T}} > 10\,\text{Gev}$ and with applied isolation criteria) of about $11 - 17\,\%$ at $8\,\text{GeV}$ going down to $3 - 7\,\%$ at $16\,\text{GeV}$. The drop can be explained by the cluster merging in the EMCal, but generally the values are very low. Since this is the case for both the invariant mass reconstruction yield and the true MC validated spectrum, this cannot be attributed to a failure of the invariant mass method and must therefore be related to the isolation criteria itself.

Even though, up until now, the presented results seem to indicate several issues with the invariant mass method, the next chapter presents and briefly discusses the application on real data to at least get an impression of the quality of the invariant mass distributions for isolated cluster yields.

6. Data Analysis

The underlying data was taken from pp collisions in 2016 at an energy of $\sqrt{s} = 13\,\text{TeV}$. Conveniently, the data is divided into so called *periods* that represent approximately a month of data collection. Two of these periods are analysed in this chapter, named LHC16k and LHC16l. The EG1 trigger was active throughout these periods with threshold values of 6 GeV (LHC16l) and 9 GeV (LHC16k). Only these triggered events were taken into account in order to increase the probability of prompt photon productions within the analysed events.

6.1. Minimum Contamination of the Raw Isolated Photon Yield

This chapter determines what could be called a minimum contamination rate of the isolated photon yield. As the cluster yield is expected to include a good share of prompt photons and fragmentation photons[8], the relative contribution of π^0 decay photons should be significantly smaller. The invariant mass distributions per p_T-bin can be found in appendix A.2 and A.3. Figure 6.1 and 6.2 present the results. The general course of the ratios looks very similar to the results that have been extracted from the jet-jet Monte Carlo analysis. The 16k-data shows a distinctly different behaviour before the jump, caused by a higher trigger value of 9 GeV in comparison to the threshold of 7 GeV used in the jet-jet Monte Carlo. This assumption is in accordance with the results for the 6 GeV-triggered 16l-data that match the previously presented results as far as the general form is concerned. From 10 GeV onwards, the ratios fall as expected and appear to be very congruent, as should be the case. In figure 6.3, the ratio between the two contamination rates is depicted to underline the accordance of the two datasets for values of $p_T > 10\,\text{GeV}$. Assuming the invariant mass method works well above 10 GeV, the contribution of reconstructible π^0 decay photons at the isolation radius of $R_\text{iso} = 0.4$ could be estimated to be around 2.5 % at 10 GeV. This, using a corresponding reconstruction efficiency of 11 %, extrapolates to a total π^0 decay photon contamination of $\frac{2.5\,\%}{0.11} \approx 22\,\%$.
The fluctuation of the data, however, increases for large isolation cones, as can also be seen in the ratio on figure 6.3. Especially at high p_T-bins the merged clusters lead to a lack of statistics. With more statistics, however, there seems to be a good chance of getting more reliable results.

[8] Fragmentation photons have been underrepresented in the Monte Carlo due to a trigger on decay photons.

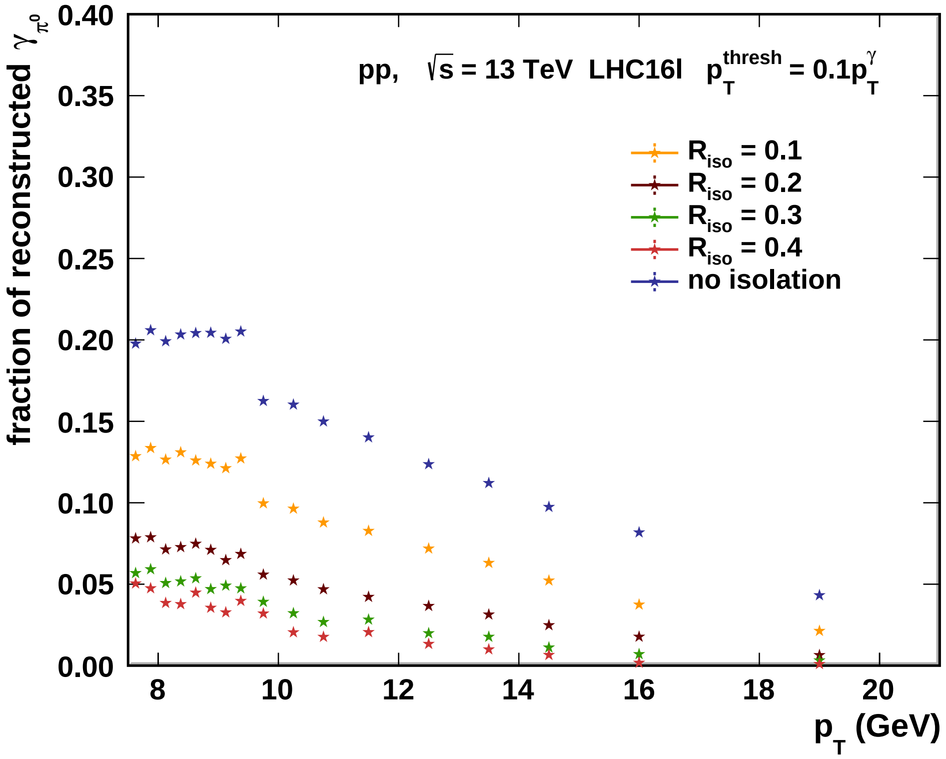

Figure 6.1.: Minimum contamination rates for different isolation cone sizes (data from LHC16l).

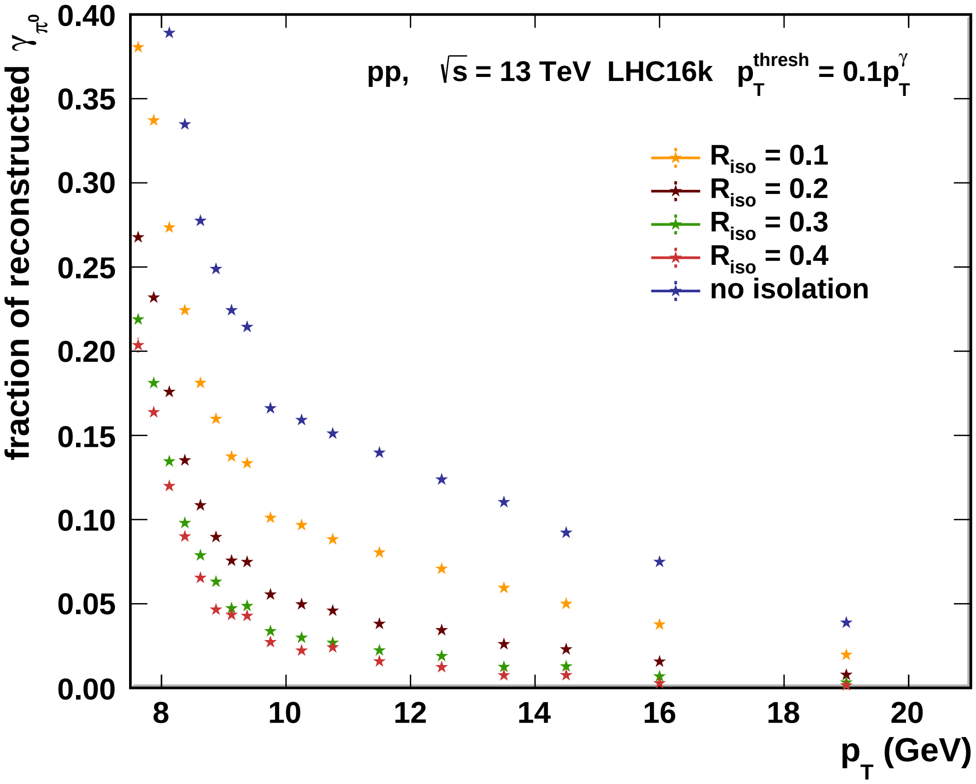

Figure 6.2.: Minimum contamination rates for different isolation cone sizes (data from LHC16k).

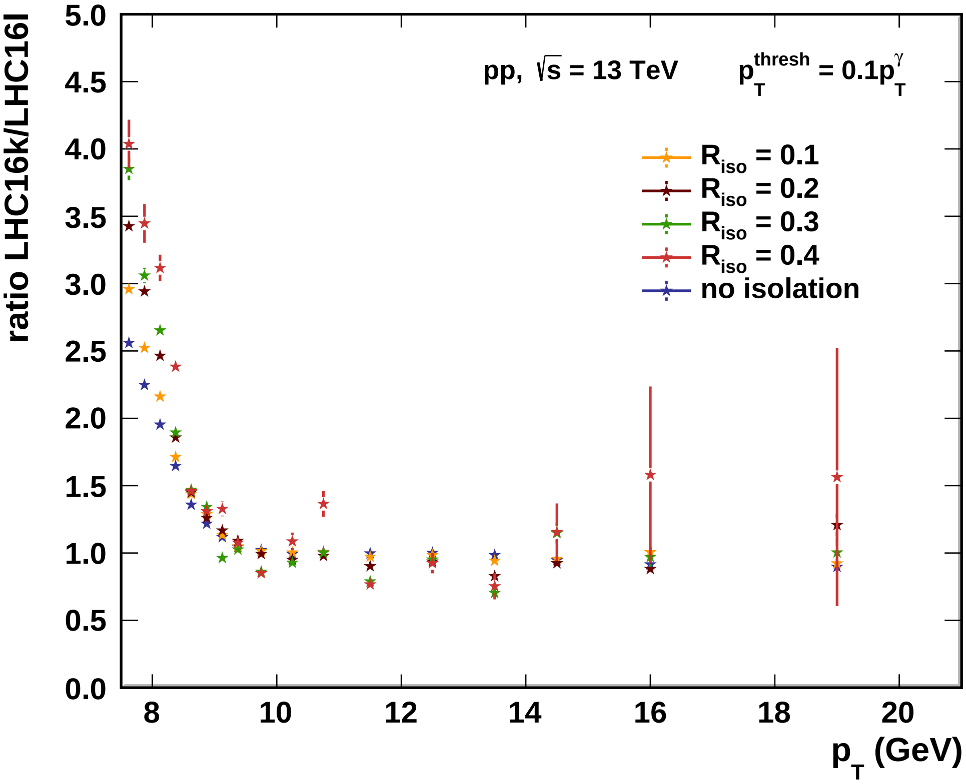

Figure 6.3.: Ratio of the two contamination rates.

7. Conclusion and Outlook

Within the scope of this thesis, it has been possible to evaluate different isolation criteria (using an energy dependent threshold and four different cone sizes) based on their efficiency and their ability to suppress background clusters via a Monte Carlo analysis. The results have shown that the use of a very small radius ($R_{iso} = 0.1$) leads to a small purity, but from there the increase of the radius by 0.1 already changes the background rejection ability substantially. The choice between $R_{iso} = 0.3$ and $R_{iso} = 0.4$ cannot be properly assessed, because the higher background suppression at $R_{iso} = 0.4$ and the better efficiency at $R_{iso} = 0.3$ could lead to similar purities dependent on the signal-to-noise ratio of the inclusive cluster yield.

Furthermore, an invariant mass analysis has been carried out on the raw isolated cluster yield in order to obtain a data driven measure for prompt photon purities. This method has been evaluated using the Monte Carlo truth output, which has revealed some underlying problem during the reconstruction of the decay photon yield, which has not been solved so far. Thus, all ratios and yields that have been determined via the invariant mass reconstruction cannot be treated as very reliable.

Nevertheless, a comparison of the contribution of reconstructed decay photons with the corresponding Monte Carlo truth suggests an accordance of the two ratios at $p_T > 10\,\mathrm{GeV}$ for isolated yields. Due to other discrepancies, however, this has to be interpreted carefully, as long as no explanation for the observable deviations has been found.

The results from applying the invariant mass method to real data fit to the expectations arising from difficulties encountered during the Monte Carlo validation. The ratios show a similar form but are shifted to lower values, thus indicating the prompt photon signal within the isolated cluster yields in the data. At an isolation radius of $R_{iso} = 0.4$, however, a clear lack of statistics further restricts the reliability of the results. Therefore, generally, the choice of an isolation cone of $R_{iso} = 0.3$ (where significantly more statistics are available), in comparison to the standard cone size of $R_{iso} = 0.4$, could be seen as an equally well criterion for measuring prompt photons. It could provide a higher efficiency for the prompt photon signal, and also a way to determine a contamination that is not purely Monte Carlo based.

In order to get more reliable results using the invariant mass reconstruction method, a refinement of the fit function might be necessary, as well as several checks for possible binning issues. In terms of the fit function, it would be easy to try the procedure with 8 TeV data in order to see if that leads to better results.

Most isolated photon analyses employ the V1 clusteriser and subsequently use the shape cut or the number of local maxima (NLM) in a cluster to reject background. Therefore, many of the merged clusters (caused by decay photons) that are separated by the V2 clusteriser will retain their oval shape (or multiple local maxima) with the V1 clusteriser and, as such, get rejected by the shape cut or the NLM cut. Using the V2 clusteriser, such clusters might get separated into two photon-like clusters and hence stay in the cluster sample, where they could be selected by the isolation criteria and then be recognized as decay photon by the invariant mass method. Due to these differences during the cluster selection process, the remaining isolated raw yields could turn out very differently. Using the V2 clusteriser in combination with the invariant mass reconstruction for purity estimation could therefore lead to a validation method for other isolated photon measurements.

Generally, it would also be interesting to vary the energy threshold in combination with the radii $R_{iso} = 0.3$ and $R_{iso} = 0.4$.

A. Invariant Mass Distributions

A.1. π^0 Decay Photons for Jet-Jet MC

A.1.1. No Isolation

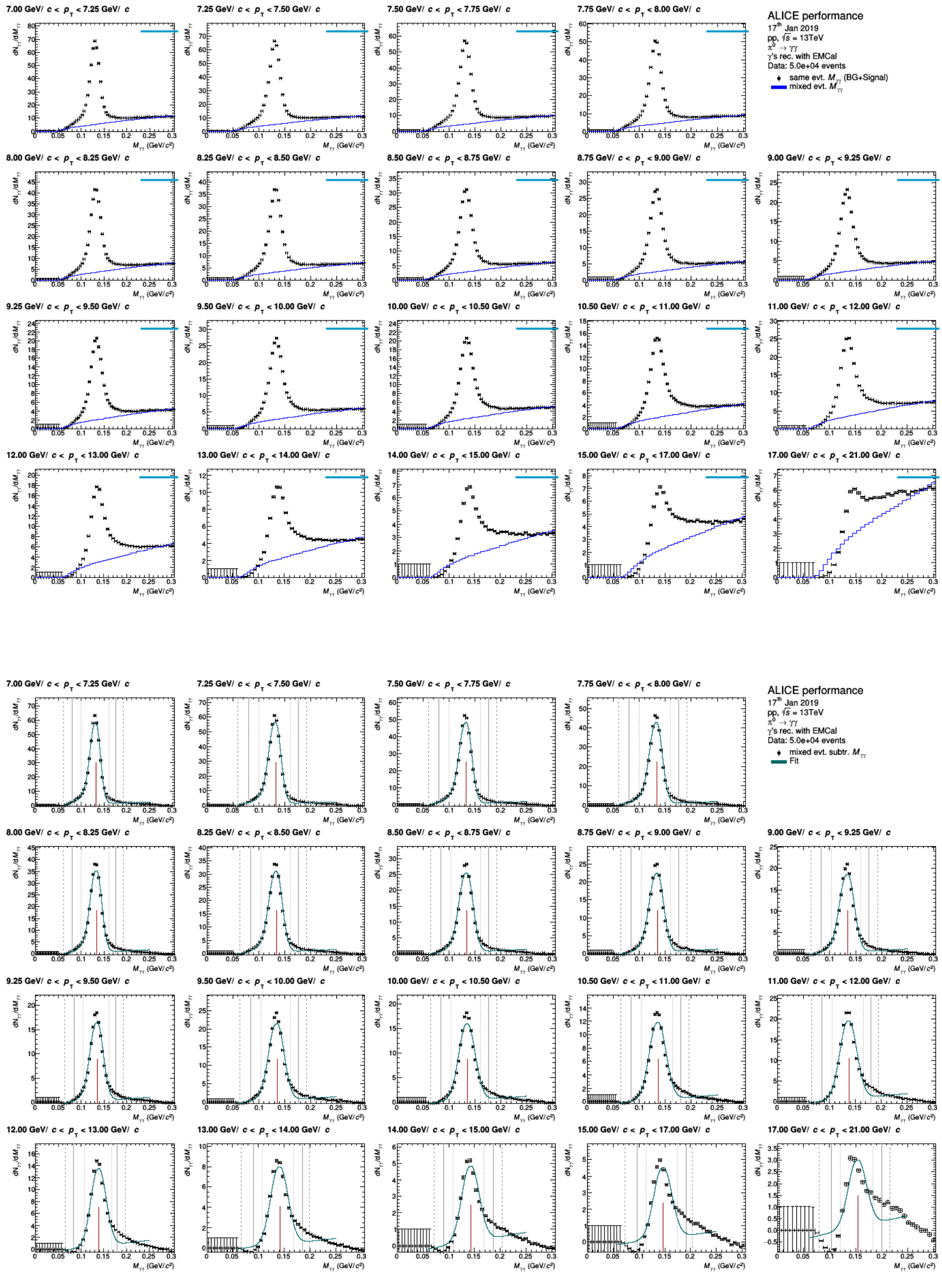

Figure A.1.: Invariant mass distributions for all chosen p_{T}-bins without isolation applied. The scaled mixed event background can be seen as a blue line (top) and the Gaussian fit together with the integration limits (bottom).

A.1.2. $R_{\text{iso}} = 0.1$

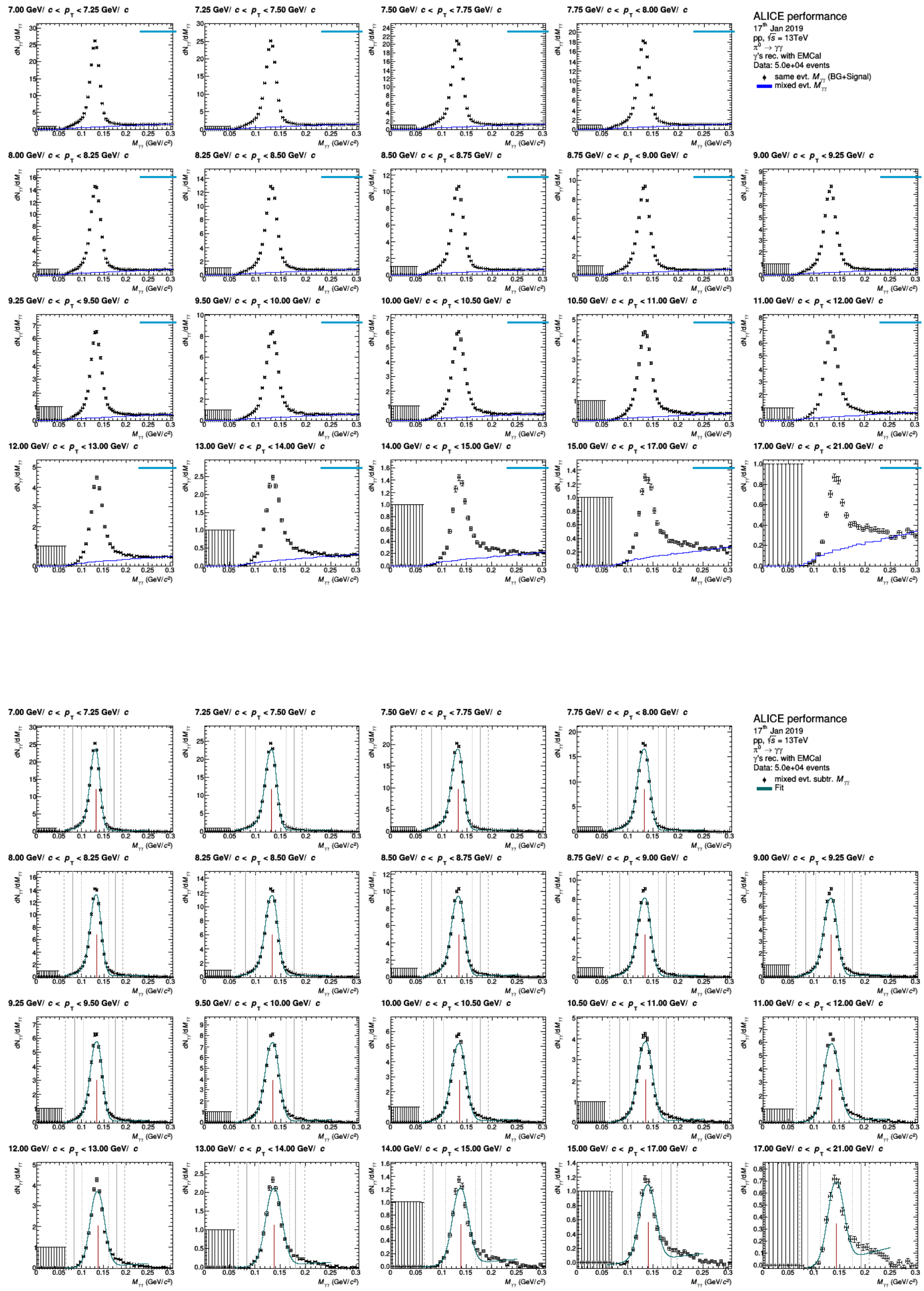

Figure A.2.: Invariant mass distributions for all chosen p_{T}-bins at $R_{\text{iso}} = 0.1$ applied. The scaled mixed event background can be seen as a blue line (top) and the Gaussian fit together with the integration limits (bottom).

A.1.3. $R_{\text{iso}} = 0.2$

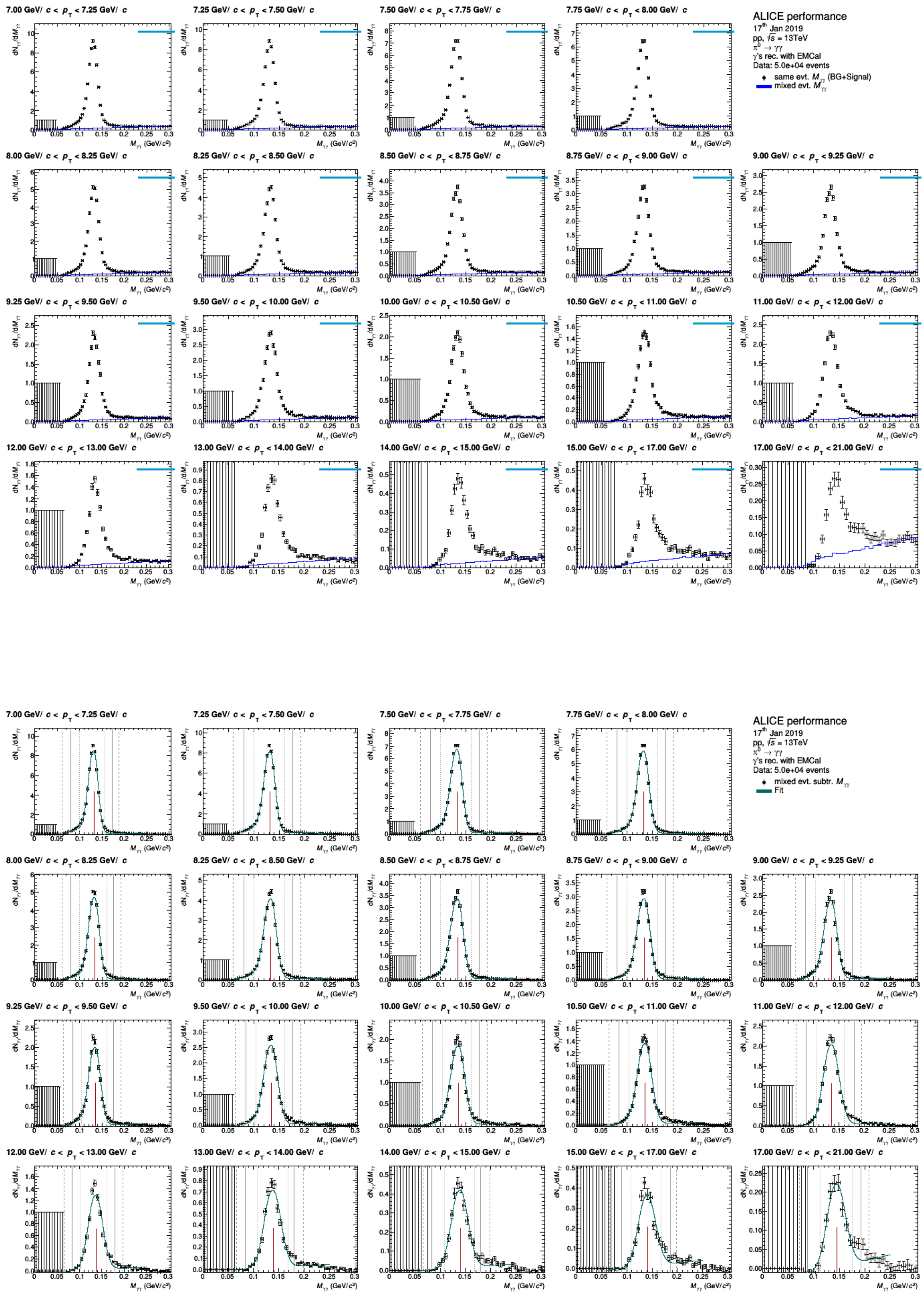

Figure A.3.: Invariant mass distributions for all chosen p_{T}-bins at $R_{\text{iso}} = 0.2$ applied. The scaled mixed event background can be seen as a blue line (top) and the Gaussian fit together with the integration limits (bottom).

A.1.4. $R_{\text{iso}} = 0.3$

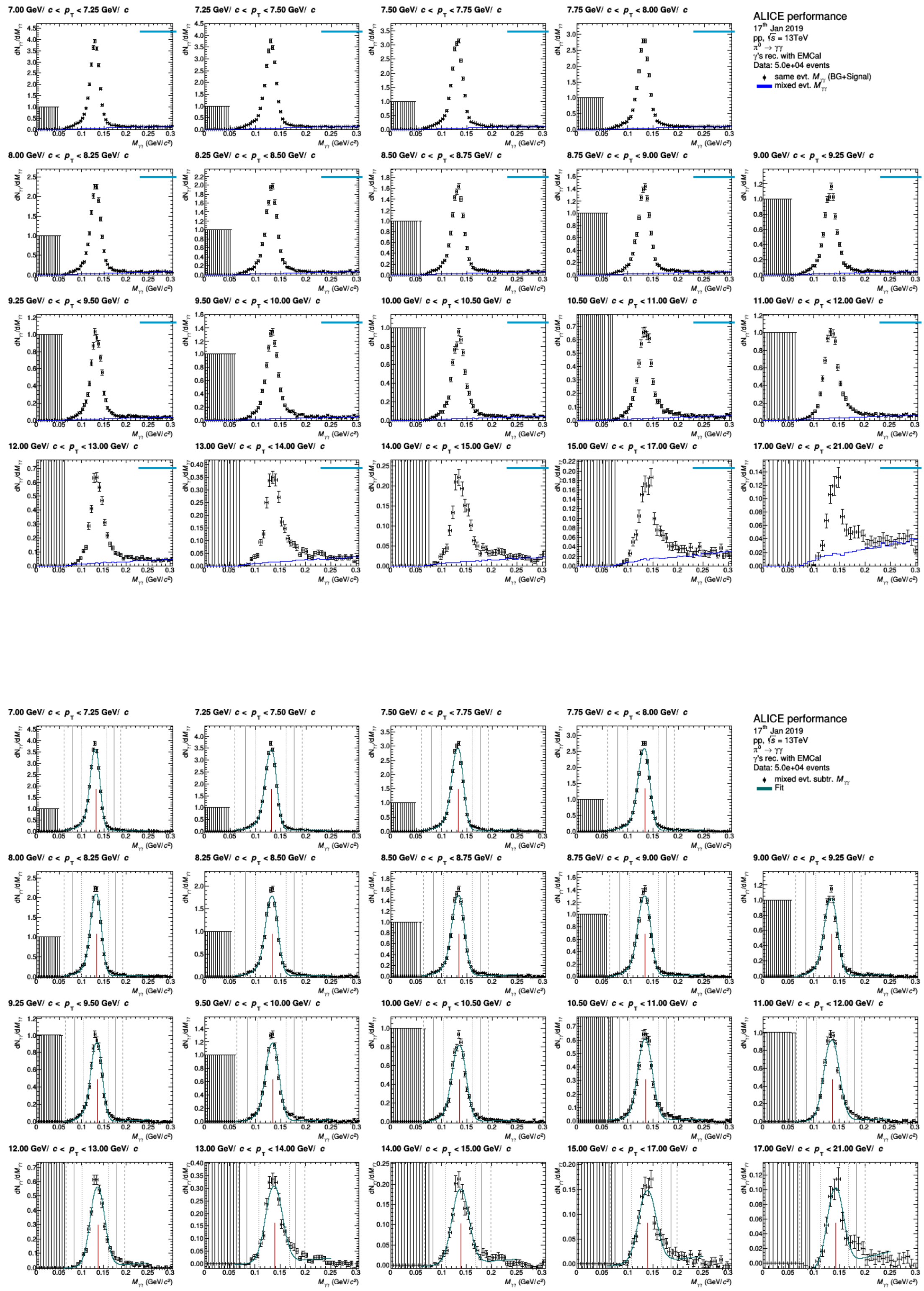

Figure A.4.: Invariant mass distributions for all chosen p_{T}-bins at $R_{\text{iso}} = 0.3$ applied. The scaled mixed event background can be seen as a blue line (top) and the Gaussian fit together with the integration limits (bottom).

A.1.5. $R_{\text{iso}} = 0.4$

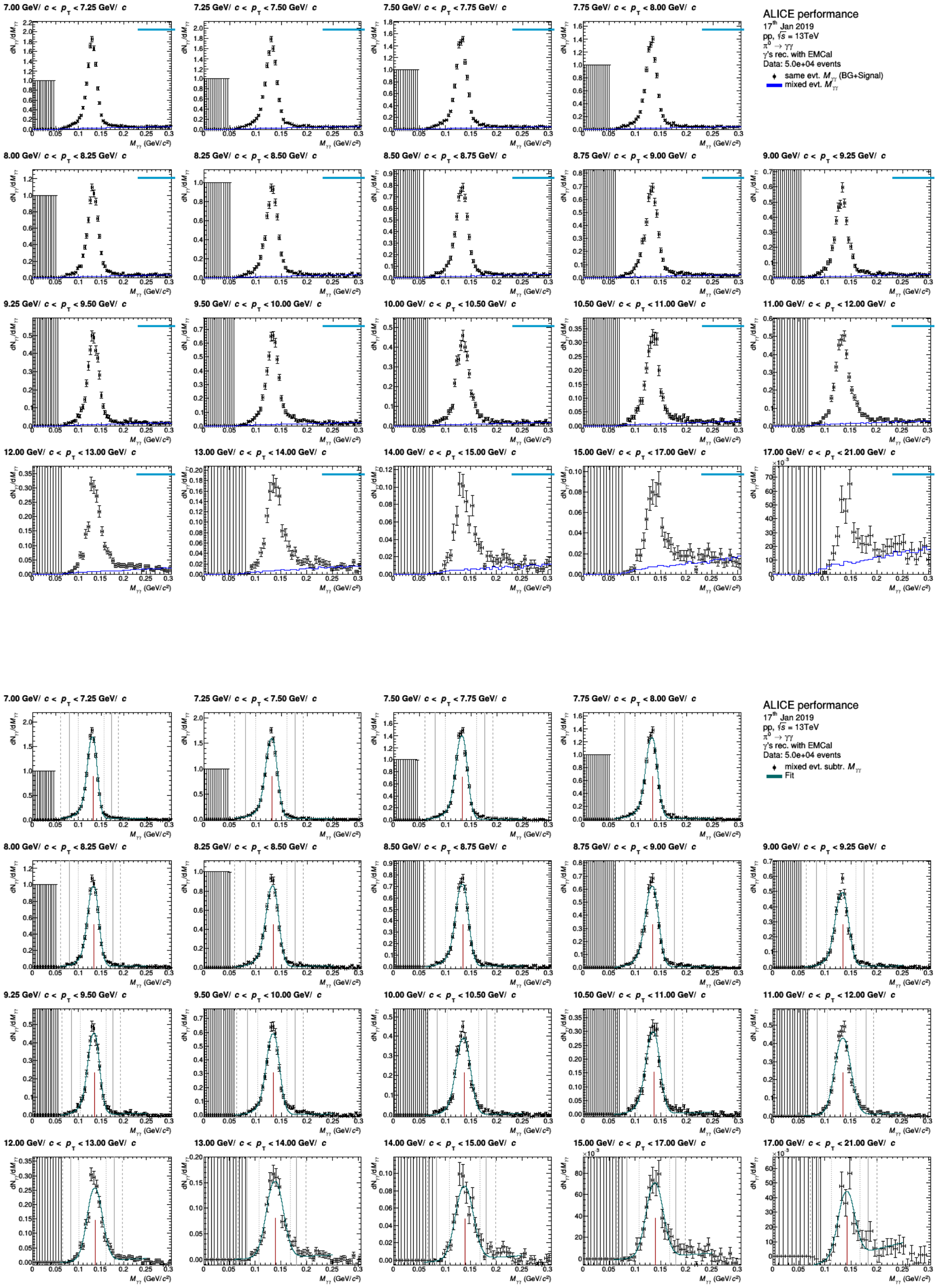

Figure A.5.: Invariant mass distributions for all chosen p_{T}-bins at $R_{\text{iso}} = 0.4$ applied. The scaled mixed event background can be seen as a blue line (top) and the Gaussian fit together with the integration limits (bottom).

A.2. π^0 Decay Photons for LHC16k

A.2.1. No Isolation

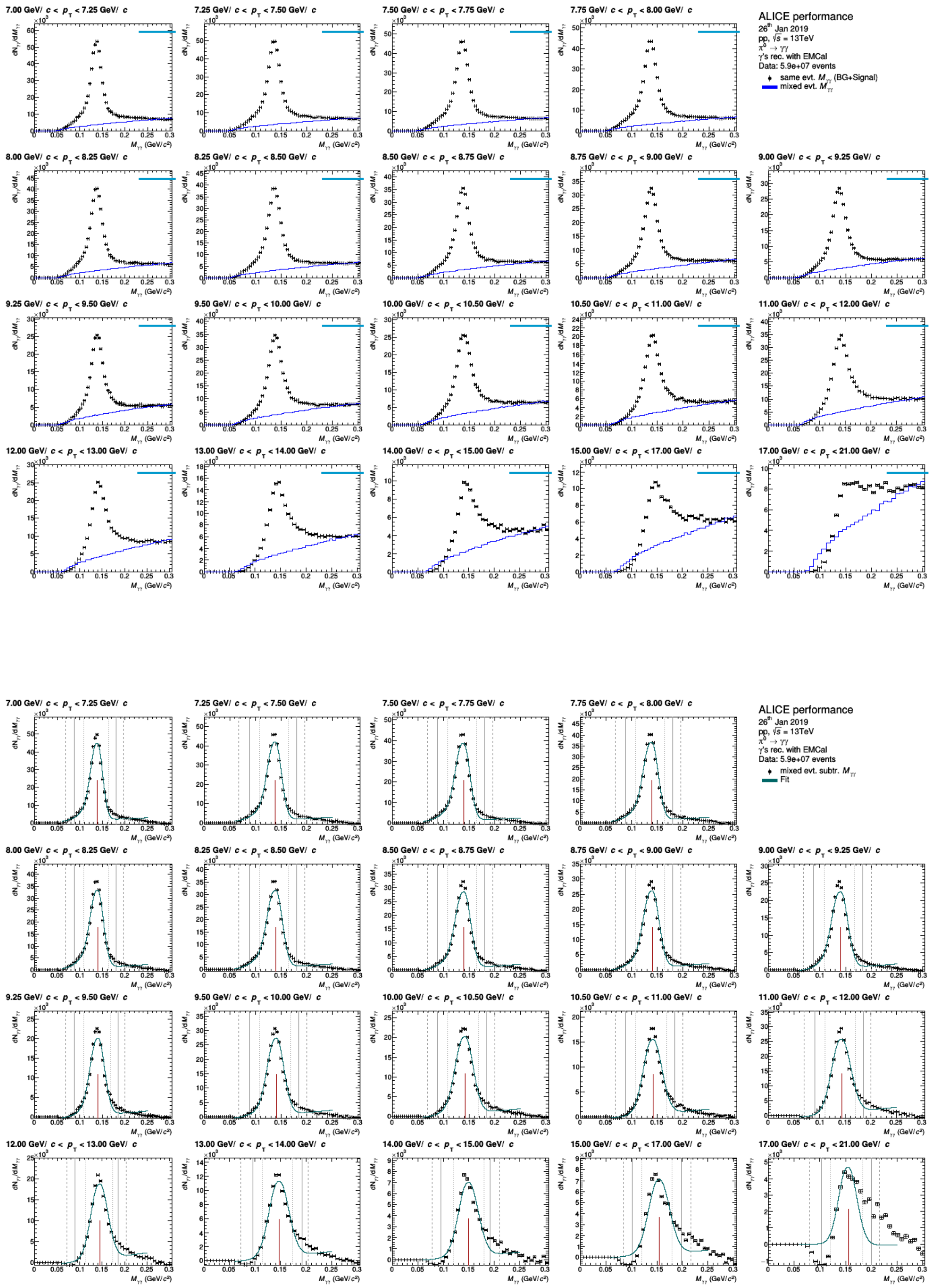

Figure A.6.: Invariant mass distributions for all chosen p_{T}-bins without isolation applied. The scaled mixed event background can be seen as a blue line (top) and the Gaussian fit together with the integration limits (bottom).

A.2.2. $R_{\text{iso}} = 0.1$

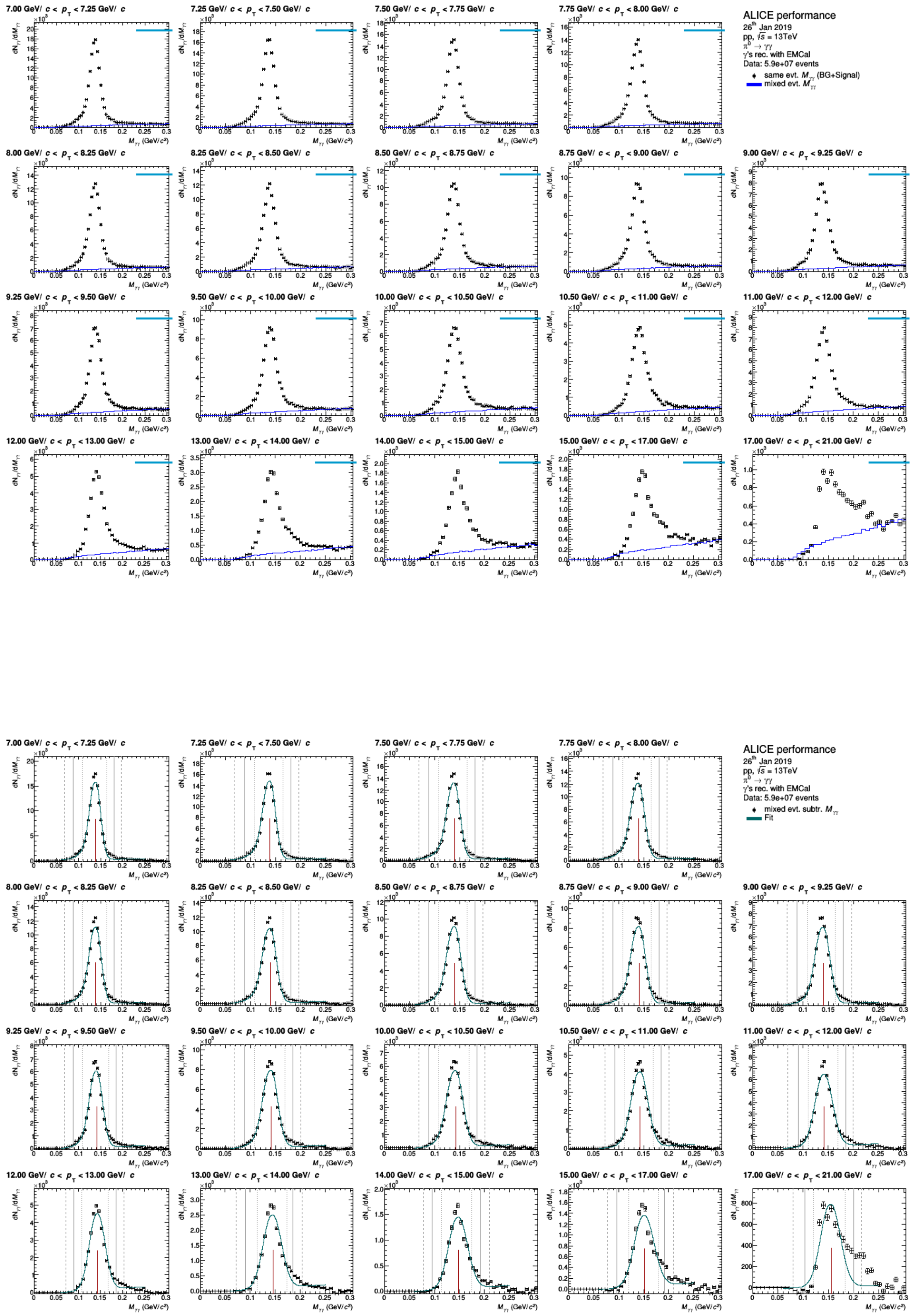

Figure A.7.: Invariant mass distributions for all chosen p_{T}-bins at $R_{\text{iso}} = 0.1$ applied. The scaled mixed event background can be seen as a blue line (top) and the Gaussian fit together with the integration limits (bottom).

A.2.3. $R_{\text{iso}} = 0.2$

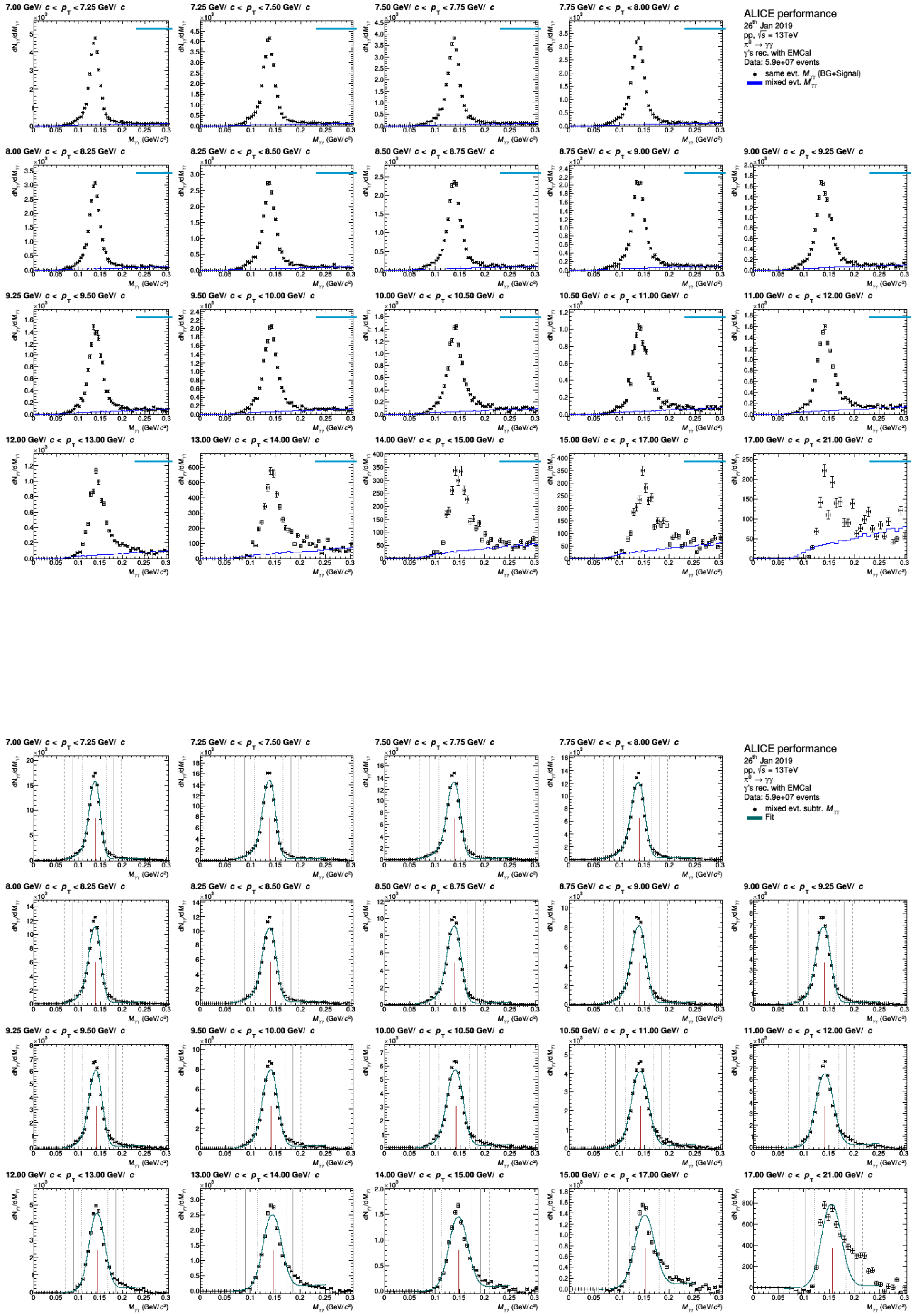

Figure A.8.: Invariant mass distributions for all chosen p_{T}-bins at $R_{\text{iso}} = 0.1$ applied. The scaled mixed event background can be seen as a blue line (top) and the Gaussian fit together with the integration limits (bottom).

A.2.4. $R_{\mathrm{iso}} = 0.3$

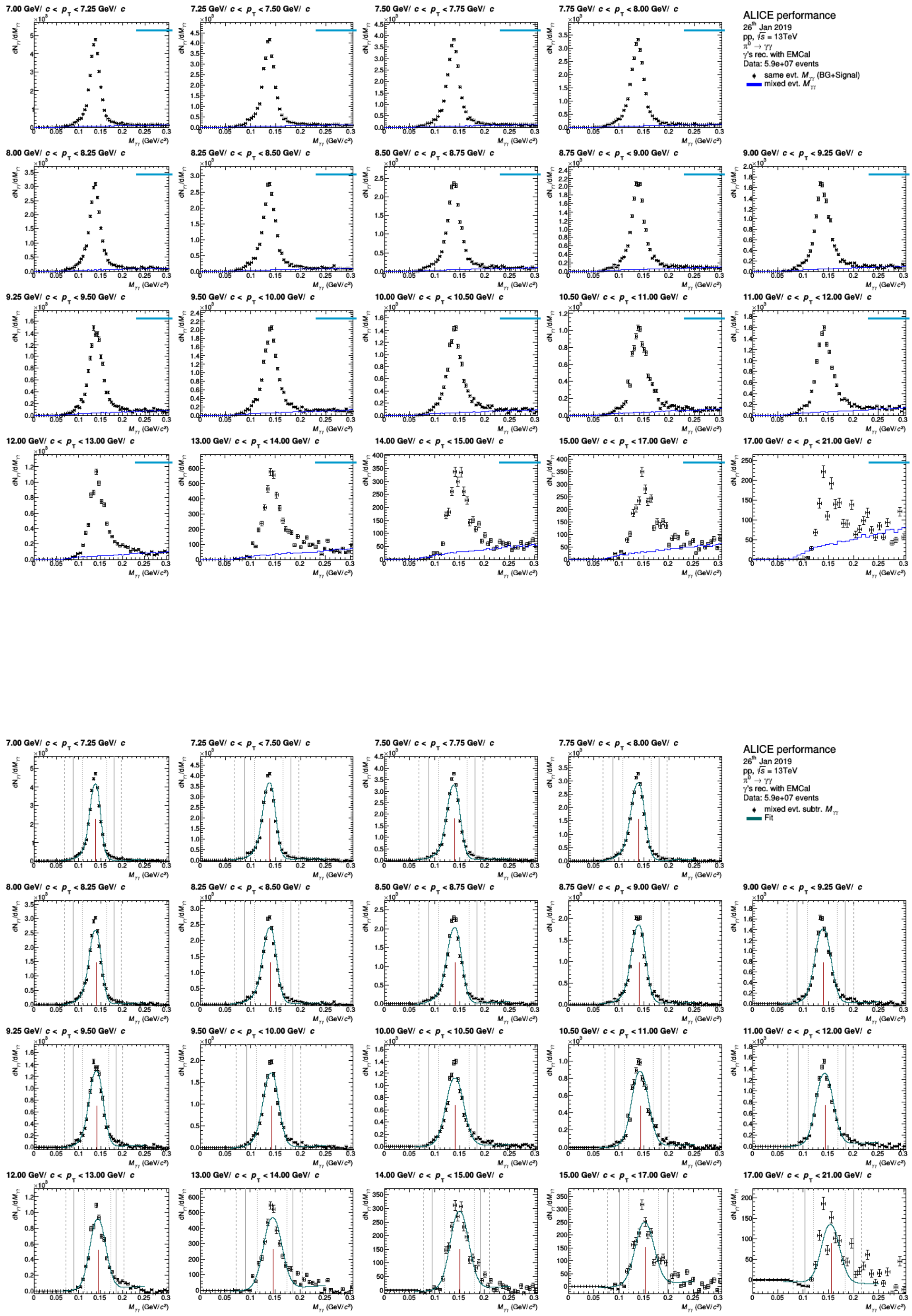

Figure A.9.: Invariant mass distributions for all chosen p_{T}-bins at $R_{\mathrm{iso}} = 0.3$ applied. The scaled mixed event background can be seen as a blue line (top) and the Gaussian fit together with the integration limits (bottom).

A.2.5. $R_{\text{iso}} = 0.4$

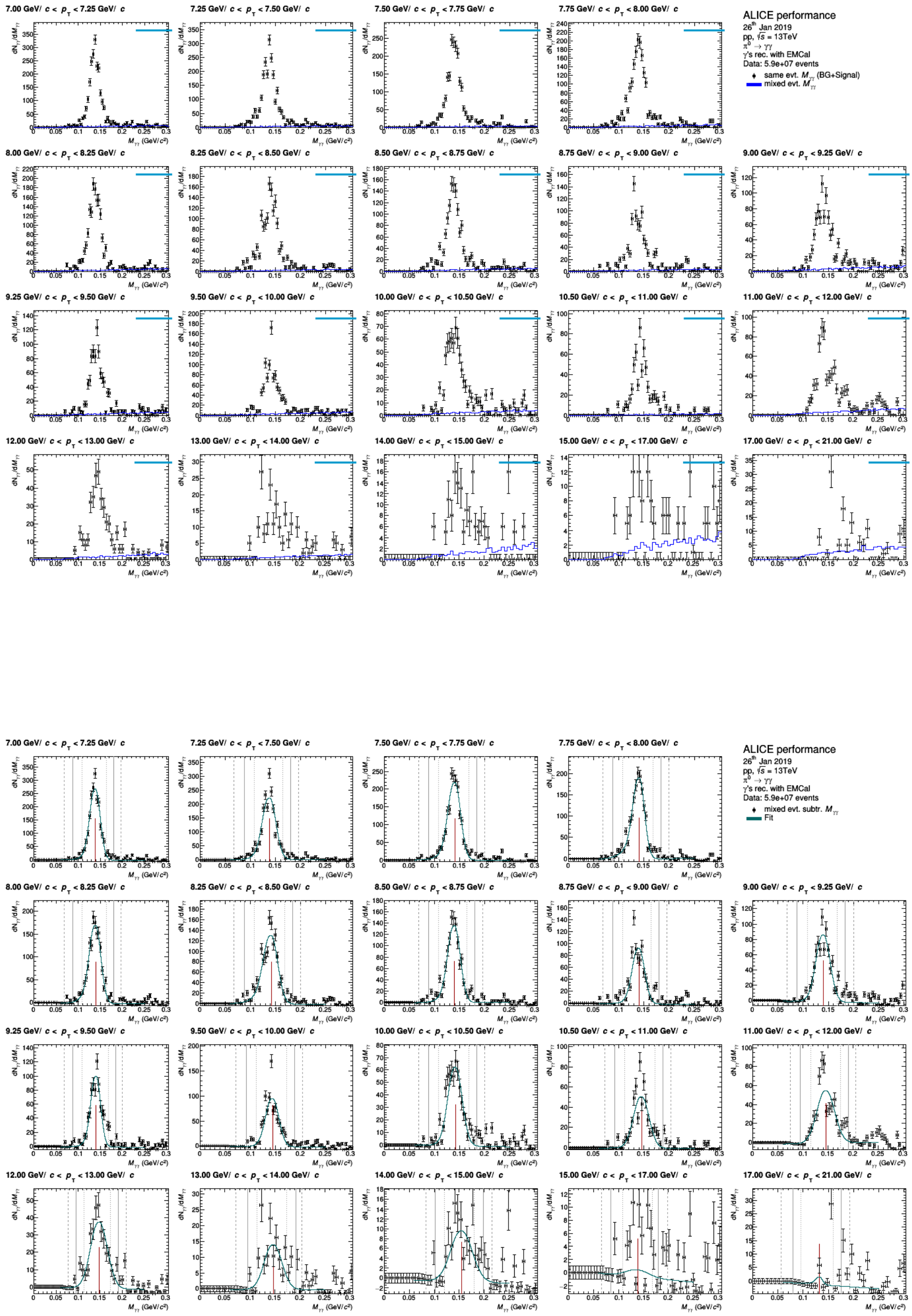

Figure A.10.: Invariant mass distributions for all chosen p_{T}-bins at $R_{\text{iso}} = 0.4$ applied. The scaled mixed event background can be seen as a blue line (top) and the Gaussian fit together with the integration limits (bottom).

A.3. π^0 Decay Photons for LHC16l

A.3.1. No Isolation

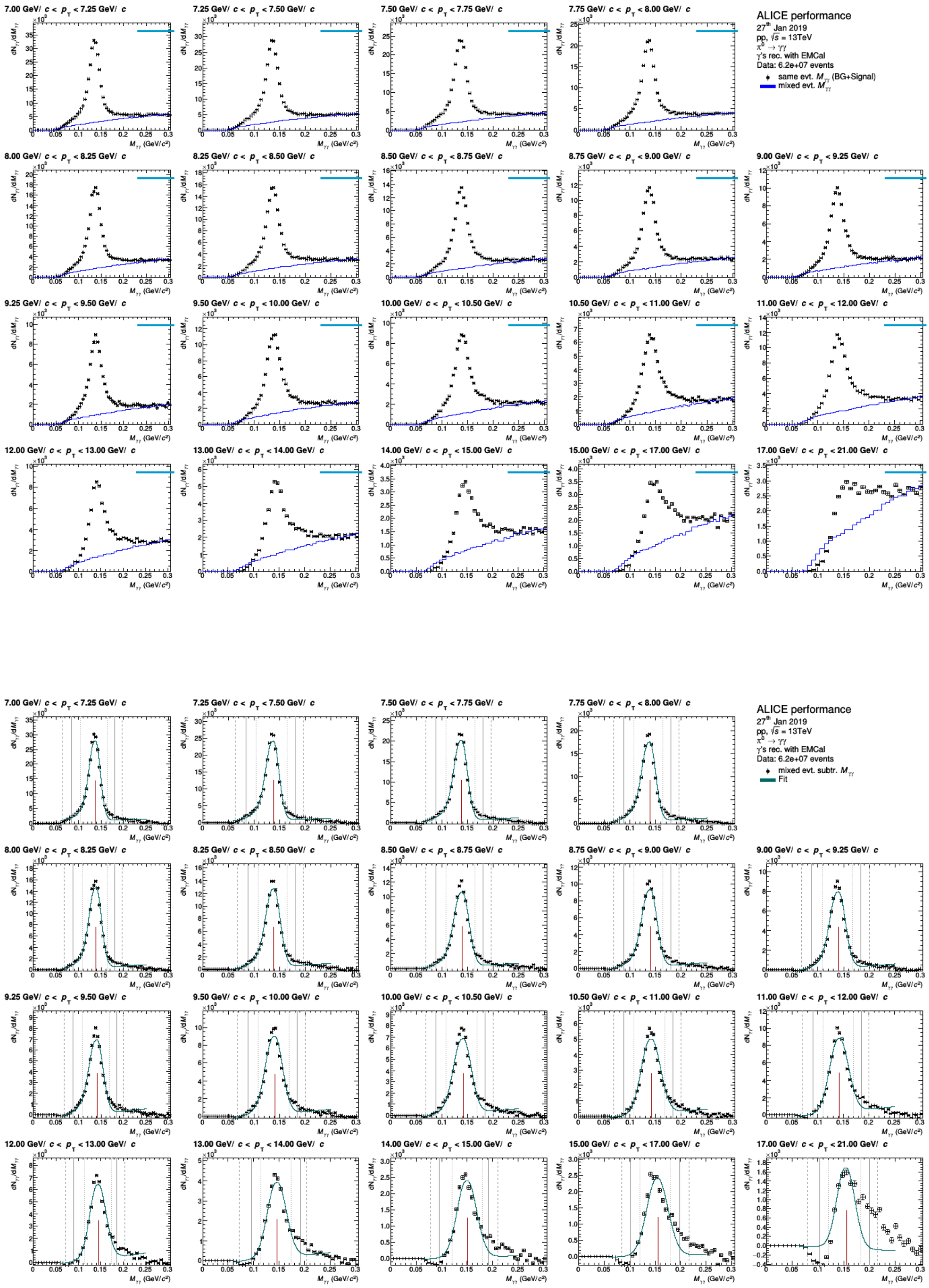

Figure A.11.: Invariant mass distributions for all chosen p_{T}-bins without isolation applied. The scaled mixed event background can be seen as a blue line (top) and the Gaussian fit together with the integration limits (bottom).

A.3.2. $R_{\mathrm{iso}} = 0.1$

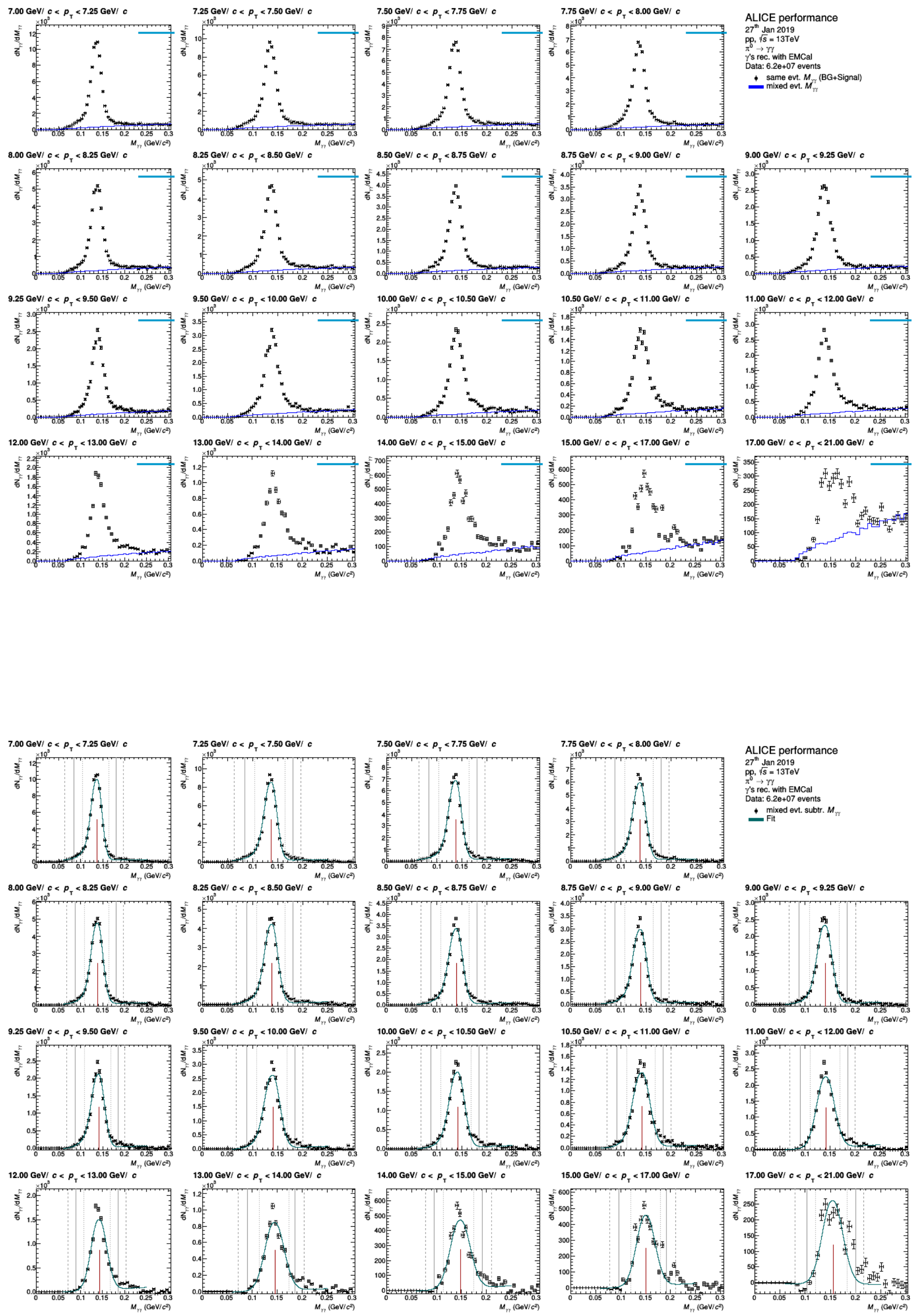

Figure A.12.: Invariant mass distributions for all chosen p_{T}-bins at $R_{\mathrm{iso}} = 0.1$ applied. The scaled mixed event background can be seen as a blue line (top) and the Gaussian fit together with the integration limits (bottom).

A.3.3. $R_{\text{iso}} = 0.2$

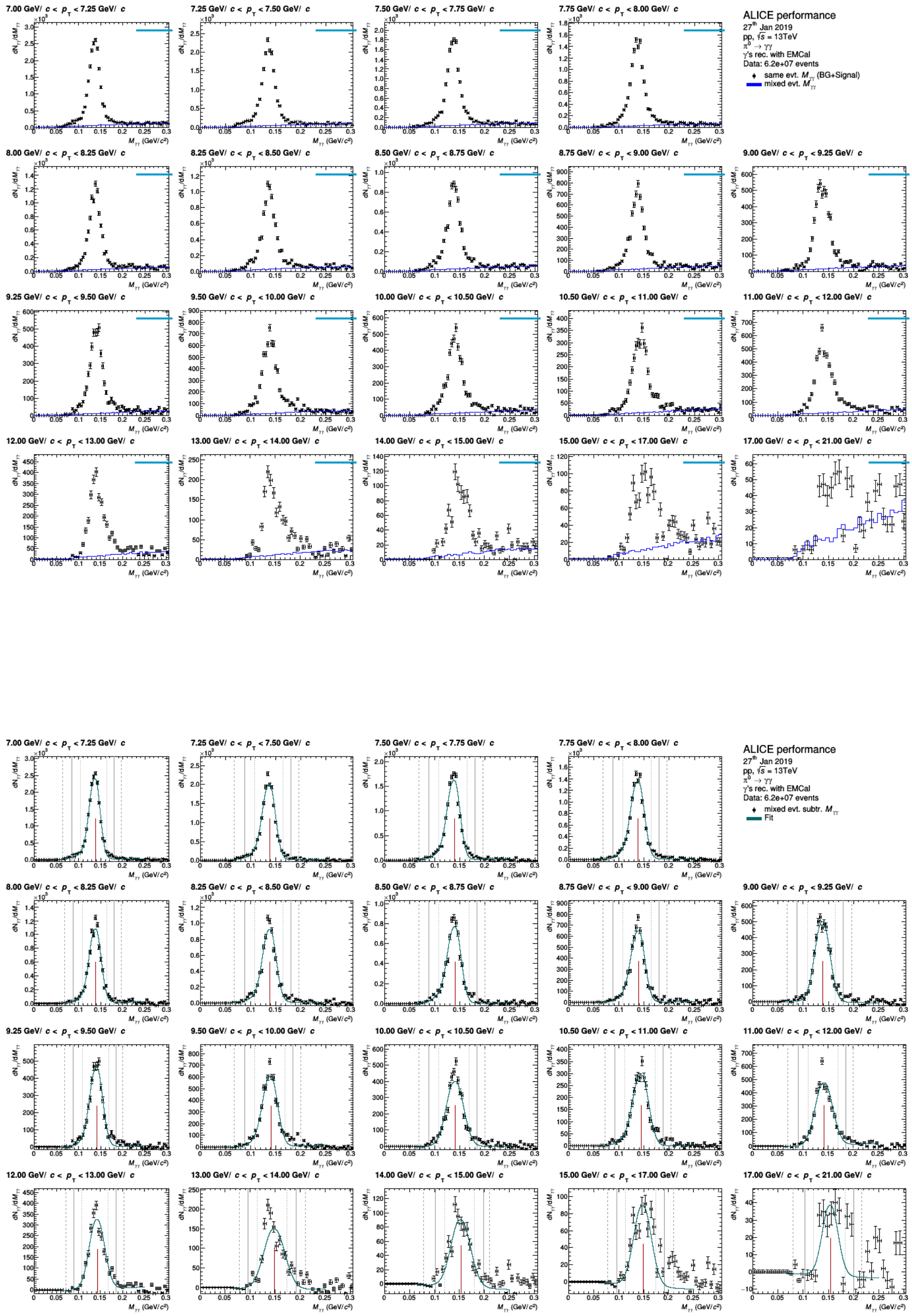

Figure A.13.: Invariant mass distributions for all chosen p_{T}-bins at $R_{\text{iso}} = 0.2$ applied. The scaled mixed event background can be seen as a blue line (top) and the Gaussian fit together with the integration limits (bottom).

A.3.4. $R_{\text{iso}} = 0.3$

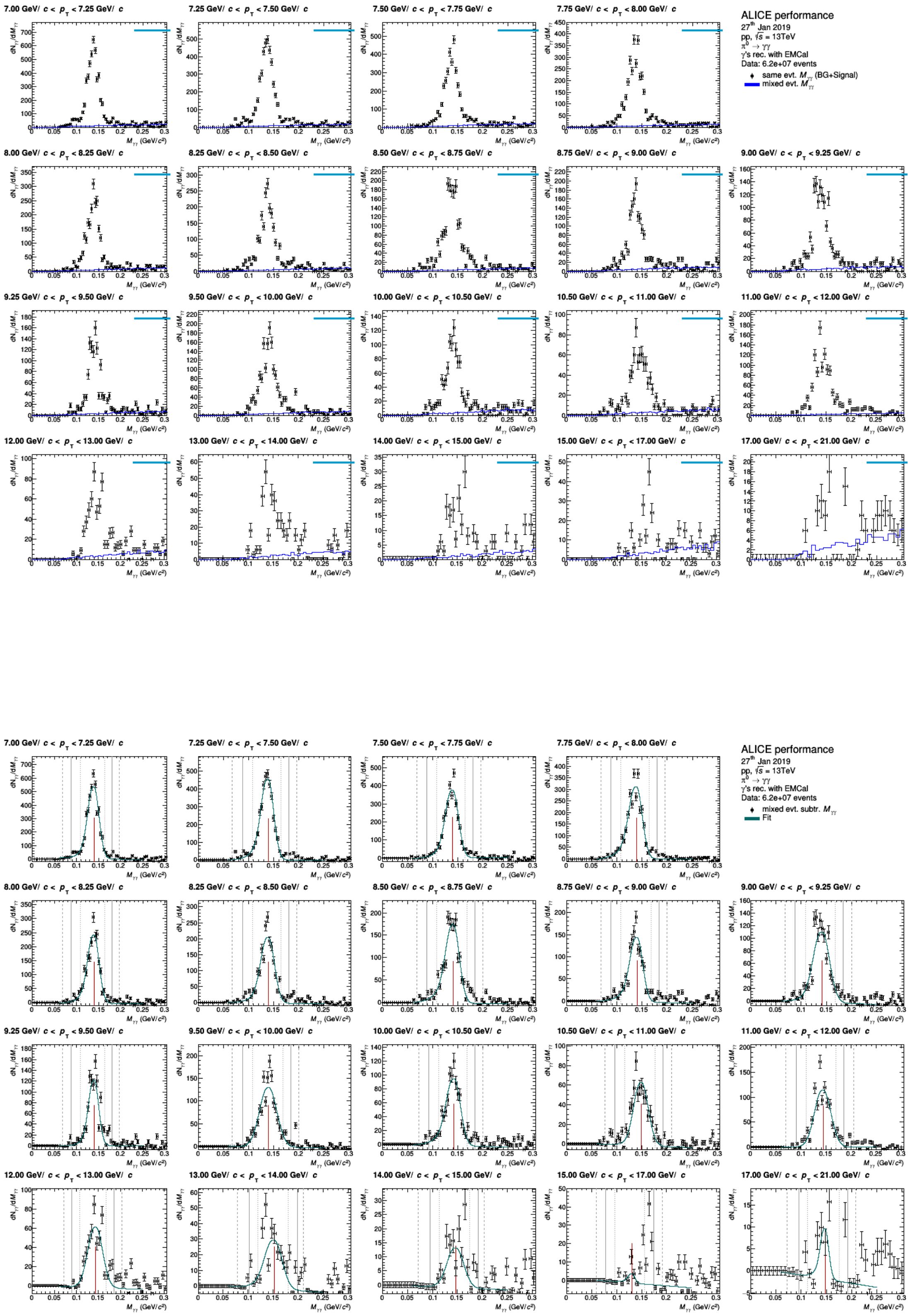

Figure A.14.: Invariant mass distributions for all chosen p_{T}-bins at $R_{\text{iso}} = 0.3$ applied. The scaled mixed event background can be seen as a blue line (top) and the Gaussian fit together with the integration limits (bottom).

A.3.5. $R_{\mathrm{iso}} = 0.4$

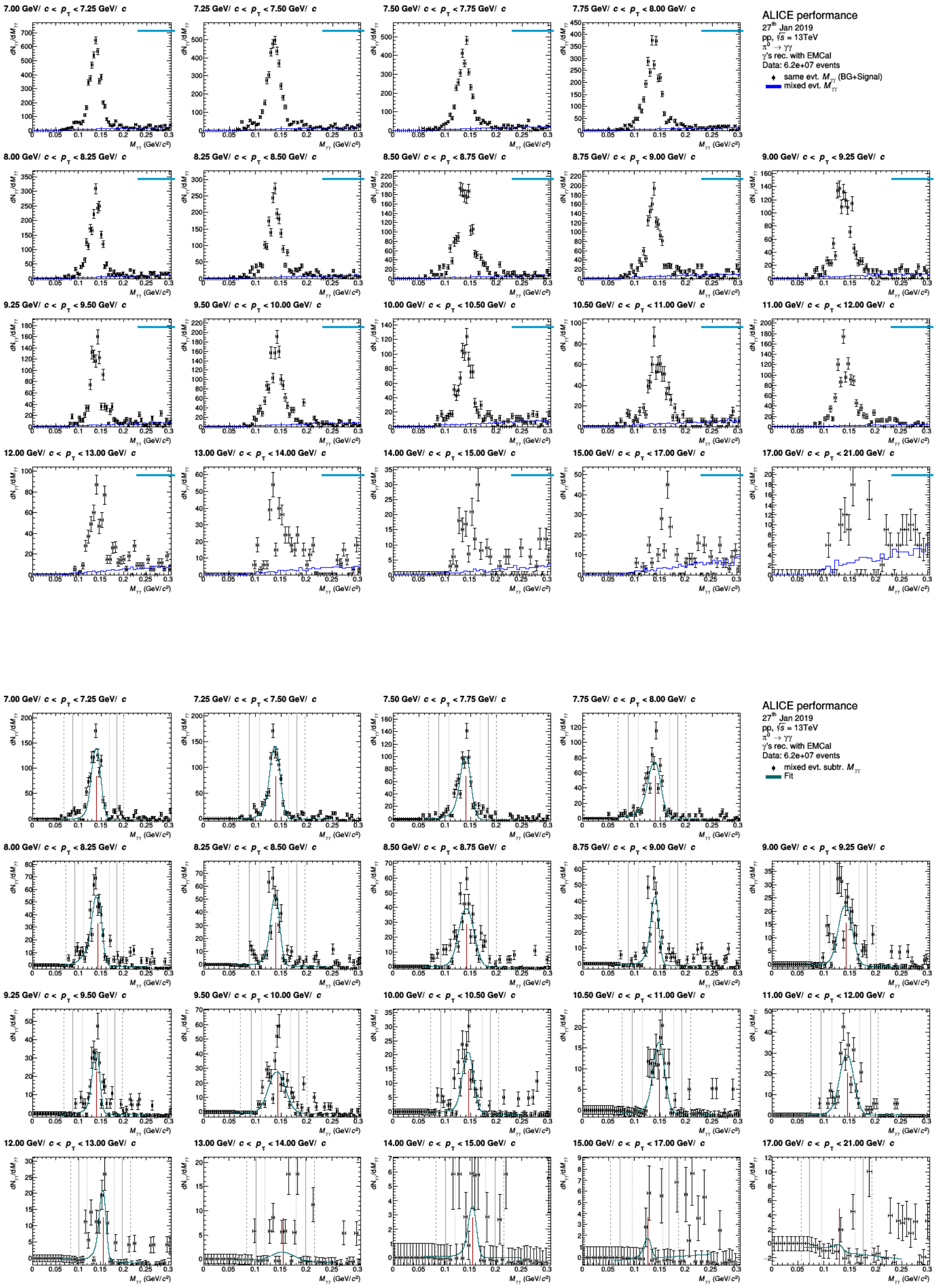

Figure A.15.: Invariant mass distributions for all chosen p_{T}-bins at $R_{\mathrm{iso}} = 0.4$ applied. The scaled mixed event background can be seen as a blue line (top) and the Gaussian fit together with the integration limits (bottom).

Bibliography

[A+10] Abeysekara, U. et al.: *ALICE EMCal Physics Performance Report.* 2010.

[A+13] Abbas, E. et al.: *Performance of the ALICE VZERO system.* JINST, 8:P10016, 2013.

[A+14] Abelev, Betty Bezverkhny et al.: *Performance of the ALICE Experiment at the CERN LHC.* Int. J. Mod. Phys., A29:1430044, 2014.

[A+18] Acharya, Shreyasi et al.: *Direct photon production at low transverse momentum in proton-proton collisions at $\sqrt{\mathbf{s}} = \mathbf{2.76}$ and 8 TeV.* 2018.

[B+12] Bazavov, A. et al.: *The chiral and deconfinement aspects of the QCD transition.* Phys. Rev., D85:054503, 2012.

[B+14] Burke, Karen M. et al.: *Extracting the jet transport coefficient from jet quenching in high-energy heavy-ion collisions.* Phys. Rev., C90(1):014909, 2014.

[B+16a] Balbastre, Gustavo Conesa et al.: *Isolated γ-hadron correlations with EMCal in pp collisions at $\sqrt{s} = 7$ TeV in 2011 data.* Alice Analysis Notes, **ALICE-ANA-2016-976**, 2016.

[B+16b] Balbastre, Gustavo Conesa et al.: *π^0 identification with EMCAL via shower shape and cluster splitting analysis methods in ALICE: 2011 data, pp and Pb-Pb collisions Feasibility studies.* Alice Analysis Notes, **ALICE-ANA-2013-589**, 2016.

[BACB+13] Bourrion, O., N. Arbor, G. Conesa-Balbastre, C. Furget, R. Guernane and G. Marcotte: *The ALICE EMCal L1 trigger first year of operation experience.* JINST, 8:C01013, 2013.

[Ben16] Bencedi, Gyula: *Nuclear modification factor of charged particles and light-flavour hadrons in p-Pb collisions measured by ALICE.* In *Proceedings, 51st Rencontres de Moriond on QCD and High Energy Interactions: La Thuile, Italy, March 19-26, 2016*, pages 285–288, 2016.

[Ber06] Berger, C.: *Elementarteilchenphysik.* Springer Verlag, 2006.

[C+04] Cortese, P et al.: *ALICE technical design report on forward detectors: FMD, T0 and V0.* 2004.

[C+08] Cortese, P. et al.: *ALICE electromagnetic calorimeter technical design report.* 2008.

[CER] CERN: *The Large Electron-Positron Collider*, January. https://home.cern/science/accelerators/large-electron-positron-collider.

[CER06] CERN, Communication Group: *LHC Guide.* CERN-Brochure-2006-003-Eng, 2006. http://cdarve.web.cern.ch/cdarve/Publications_CD/CERN_brochure-2006-003-eng.pdf.

[CER13] CERN: *LHCb*, October 2013. https://home.cern/science/experiments/lhcb.

[CER18] CERN: *The Large Hadron Collider*, 2018. https://home.cern/science/accelerators/large-hadron-collider.

[Col] Collaboration, ALICE: *The ALICE Time Projection Chamber.* http://alice-tpc.web.cern.ch/content/alice-time-projection-chamber.

[Col08] Collaboration, ALICE: *The ALICE Experiment - Overview of a particle detector*, 2008. http://aliceinfo.cern.ch/Public/en/Chapter2/Chap2InsideAlice-en.html.

[Col15] Collaboration, EMCal: *EMCal Offline Documentation.* AliRoot/EMCAL/doc/EMCALDocumentation.pdf, **ALICE-INT 2012**, 2015.

[Col18a] Collaboration, ATLAS: *About the ATLAS Experiment*, 2018. https://atlas.cern/discover/about.

[Col18b] Collaboration, CMS: *Physics*, 2018. https://cms.cern/physics.

[D+00] Dellacasa, G. et al.: *ALICE: Technical design report of the time projection chamber.* 2000.

[DL17] De Leo, V.: *Measurement of the running of the fine structure constant below 1 GeV with the KLOE detector.* In *Proceedings, 52nd Rencontres de Moriond on QCD and High Energy Interactions: La Thuile, Italy, March 25-April 1, 2017*, pages 57–60, 2017.

[G+18] Germain, M. et al.: *Isolated directed photon cross section measurement in pp collisions at $\sqrt{s}$ = 7 TeV with the ALICE detector at LHC.* Alice Analysis Notes, **ALICE-ANA-2018-295**, 2018.

[Gri10] Griffiths, David: *Introduction to Elementary Particles.* WILEY-VCH Verlag GmbH & Co. KGaA, 2nd edition, 2010.

[Hab18] Haber, Alexander: *Multicomponent Superfluids and Superconductors in Dense Nuclear and Quark Matter.* PhD thesis, 2018.

[Id10] Ichou, Raphaelle and David d'Enterria: *Sensitivity of isolated photon production at TeV hadron colliders to the gluon distribution in the proton.* Phys. Rev., D82:014015, 2010.

[Ji] Ji, Xiangdong: *Introduction to QCD and the Standard Model.* https://www.physics.umd.edu/courses/Phys741/xji/lecture_notes.htm.

[KB13] Klein-Bösing, C.: *Study of the Quark-Gluon Plasma with Hard and Electromagnetic Probes*, 2013.

[Kur15] Kurashvili, Podist: *Photon and neutral pion production in pp and Pb-Pb collisions at LHC energies in the ALICE experiment.* In *International School on High Energy Physics: Session C: Workshop in HEP (LISHEP 2015) Manaus, Amazonas, Brazil, August 2-9, 2015*, 2015.

[Lod18] Lodato, Davide Francesco: *Measurement of the prompt photon production cross section in proton proton collisions at $\sqrt{s} = 7$ TeV with ALICE*, 2018.

[M+17] Mühlheim, D. et al.: *Neutral meson measurements with the EMCal in ALICE in pp collisions at $\sqrt{s} = 8$ TeV.* Alice Analysis Notes, **ALICE-ANA-3086**, 2017.

[Man12] Manzari, Vito: *The present Inner Tracking System - Steps forward!*, December 2012. http://alicematters.web.cern.ch/?q=ALICE_currentITS.

[oJ08] Jyvaskyla, University of: *ALICE EMCal*, 2008. https://trac.cc.jyu.fi/projects/alice/wiki/EMCAL.

[P+16] Patrignani, C. et al.: *Review of Particle Physics.* Chin. Phys., C40(10):100001, 2016.

[Pop11] Poppenborg, Hendrik: *Characterization of Heavy-Ion-Background in Jet-Reconstruction*, Sep 2011.

[PRSZ06] Povh, Bogdan, Klaus Rith, Christoph Scholz and Frank Zetsche: *Teilchen und Kerne. Eine Einführung in die physikalischen Konzepte.* Springer-Verlag GmbH, Sechste edition, 2006.

[Ron16] Ronflette, Lucile: *Isolated photon production in p-Pb collisions at with the ALICE experiment at $\sqrt{s} = 5.02$ TeV the LHC*, Nov 2016. https://cds.cern.ch/record/2242378/files/Thesis-2016-Ronflette.pdf.

[Rø09] Røed, Ketil: *Single Event Upsets in SRAM FPGA based readout electronics for the Time Projection Chamber in the ALICE experiment*, 2009.

[Sat11] Satz, Helmut: *The Quark-Gluon Plasma: A Short Introduction.* Nucl. Phys., A862-863:4–12, 2011.

[Sch17] Schach, Rene: *Messung isolierter Photonen in pp: $\sqrt{s} = 8$ TeV mit dem ALICE-EMCal Detektor*, Nov 2017. https://www.uni-frankfurt.de/69444444/MA_Schach-2017.pdf.

[Ser15] SERRA, NICOLA: *Standard Model*, April 2015. https://www.physik.uzh.ch/groups/serra/StandardModel.html.

[Sjo] SJOSTRAND, TORBJORN: *Introduction to PYTHIA*. http://home.thep.lu.se/~torbjorn/Pythia.html.

[SMS06] SJOSTRAND, TORBJORN, STEPHEN MRENNA and PETER Z. SKANDS: *PYTHIA 6.4 Physics and Manual*. JHEP, 05:026, 2006.

[SS17] SCHMIDT, CHRISTIAN and SAYANTAN SHARMA: *The phase structure of QCD*. J. Phys., G44(10):104002, 2017.

[Web17] WEBER, MICHAEL: *Pythia GJ events with gammas in EMCal /DCal+PHOS and JJ events triggered by decay photons in EMCal/DCal+PHOS*, 2017. https://alice.its.cern.ch/jira/browse/ALIROOT-7269.

[Wil05] WILCZEK, FRANK: *Asymptotic freedom: From paradox to paradigm*. Proc. Nat. Acad. Sci., 102:8403–8413, 2005. [Rev. Mod. Phys.77,857(2005)].

[X+18] XU, RAN et al.: *Isolated directed photon cross section measurement in pp collisions at $\sqrt{s}$ = 13 TeV with the ALICE detector at LHC*. Alice Analysis Notes, **ALICE-ANA-2018-849**, 2018.

[Zha16] ZHANG, YANXI: *Results on heavy ion collisions at LHCb*, March 2016. https://cds.cern.ch/record/2144919/files/LHCb-TALK-2016-045.pdf.

Acknowledgements

Ich möchte mich ganz herzlich für jegliche Unterstützung bedanken, die mir im Laufe meiner Masterarbeit widerfahren ist.

Ganz besonders bedanke ich mich bei Christian Klein-Bösing und Anton Andronic für gute Ratschläge und die Ermöglichung meiner Teilnahme an verschiedenen Konferenzen und der ELHC Summerschool, bei Daniel und Hendrik für sämtliche inhaltliche Unterstützung, bei Ian und Jana für den stetigen moralischen Beistand, bei meiner gesamten Arbeitsgruppe für eine schöne und lehrreiche Zeit, bei meiner Familie für das passende Maß an Ablenkung und Rücksichtsnahme besonders in den letzten Wochen, und bei meiner Mutter für die schönen Wanderungen und dafür, dass sie sich für meine Titelseite interessiert.

Hiermit versichere ich, dass ich die vorliegende Arbeit selbständig verfasst und keine anderen außer den angegebenen Quellen und Hilfsmitteln verwendet habe.

Münster, Januar 2019

....
(Helena Horstmann)